Targeting IRE1α improves insulin sensitivity and thermogenesis and suppresses metabolically active adipose tissue macrophages in obesity

Dan Wu[1, 2], Venkateswararao Eeda[2], Zahra Maria[2], Komal Rawal[2], Oana Herlea-Pana[2], Ram Babu Undi[3], Hui-Ying Lim[3], & Weidong Wang[1,2]*

[1]Department of Genetics, Heersink School of Medicine, UAB Comprehensive Diabetes Center, University of Alabama at Birmingham, 1918 University Blvd, Birmingham, AL, 35233, United States; [2]Department of Medicine, Division of Endocrinology, [3]Department of Physiology, Harold Hamm Diabetes Center, The University of Oklahoma Health Science Center, 941 Stanton L. Young Boulevard, Oklahoma City, Oklahoma 73104, United States

*Corresponding author: ww8@uab.edu

Abstract

Overnutrition engenders the expansion of adipose tissue and the accumulation of immune cells, in particular, macrophages, in the adipose tissue, leading to chronic low-grade inflammation and insulin resistance. In obesity, several proinflammatory subpopulations of adipose tissue macrophages (ATMs) identified hitherto include the conventional “M1-like” CD11C-expressing ATM and the newly discovered metabolically activated CD9-expressing ATM; however, the relationship among ATM subpopulations is unclear. The ER stress sensor inositol-requiring enzyme 1α (IRE1α) is activated in the adipocytes and immune cells under obesity. It is unknown whether targeting IRE1α is capable of reversing insulin resistance and obesity and modulating the metabolically activated ATMs. We report that pharmacological inhibition of IRE1α RNase significantly ameliorates insulin resistance and glucose intolerance in diet-induced obesity mice. IRE1α inhibition also increases thermogenesis and energy expenditure, and hence protects against high fat diet-induced obesity. Our study shows that the “M1-like” $CD11c^+$ ATMs are largely overlapping with but yet non-identical to $CD9^+$ ATMs in obese white adipose tissue. Notably, IRE1α inhibition diminishes the accumulation of obesity-induced metabolically activated ATMs and “M1-like” ATMs, resulting in the curtailment of adipose inflammation and ensuing reactivation of thermogenesis, without augmentation of the alternatively activated M2 macrophage population. Our findings suggest the potential of targeting IRE1α for the therapeutic treatment of insulin resistance and obesity.

Introduction

Overnutrition and obesity are closely associated with insulin resistance which serves as a common precursor to type 2 diabetes, cardiovascular diseases, non-alcoholic fatty liver disease, and other metabolic disorders. Under chronic energy overload, adipose tissue expands significantly for the storage of the excess energy in the form of lipids and this expansion coincides with the recruitment and accumulation of immune cells, in particular macrophages, in adipose tissue. Once the lipid storage capacity is reached, adipocytes can no longer incorporate lipids from the circulation but instead release fatty acids into the circulation through lipolysis. Meanwhile, the excess accumulation of immune cells in the adipose tissue leads to chronic low-grade inflammation, including aberrant proinflammatory cytokine production, in the adipose tissue (Weisberg et al., 2003; Xu et al., 2003). Both aberrant adipocyte lipolysis and adipose tissue inflammation are known to exacerbate each other (Foley et al., 2021) and are regarded as key factors contributing to insulin resistance in obesity.

The accumulated adipose tissue macrophages (ATMs) were initially thought to undergo a phenotypic polarization from an anti-inflammatory M2 to a pro-inflammatory M1 state, promoting local and systemic inflammation with the production and secretion of pro-inflammatory cytokines (Lumeng et al., 2007). However, there is a growing body of evidence that does not support this obesity-induced M1/M2 polarization model. Instead, recent studies have identified a predominant population of ATMs that emerge in obesity and present a metabolically activated phenotype (Coats et al., 2017; Kratz et al., 2014;

Xu et al., 2013). The metabolically activated ATMs have lately been shown to express CD9 and/or Trem2 by studies using unbiased single-cell RNA sequencing (Hill et al., 2018; Jaitin et al., 2019). These obesity-associated metabolically active ATMs not only potentiate inflammation but also promote dead adipocyte clearance (Coats *et al.*, 2017; Hill *et al.*, 2018; Kratz *et al.*, 2014). However, the relationship between the previously identified "M1-like" CD11c+ ATMs and the new $CD9^+$ and/or $Trem2^+$ ATM subpopulations is unclear.

The endoplasmic reticulum (ER) is a major site for protein synthesis and folding and the synthesis of lipid and sterol. When the demand for protein folding in the ER exceeds its capacity, ER stress occurs. The three ER stress sensors, inositol-requiring enzyme (IRE)-1, PKR-like ER-regulating kinase (PERK), and activating transcription factor (ATF)-6, are then activated to trigger the unfolded protein response (UPR) that initially serves as an adaptive means to resolve ER stress, but will eventually become maladaptive if the perturbation persists. IRE1α, the most evolutionarily conserved among the UPR sensors, is an ER transmembrane protein with dual serine/threonine kinase and RNase domains and once activated, can catalyze the unconventionally cleavage of XBP1 mRNA for XBP1 translation or initiate a process termed regulated IRE1-dependent decay of RNA (RIDD) (Back and Kaufman, 2012; Fonseca et al., 2011; Hetz et al., 2013; Papa, 2012). IRE1α activation was reported to induce/potentiate inflammatory cytokine production and inflammation through the control of transcriptional regulation and intracellular signaling pathways via its dual enzymatic activities (Lerner et al., 2012; Martinon et al., 2010; Oslowski et al., 2012). ER stress and IRE1α activation has been reported in both human and rodent obese adipose tissues (Boden et al.,

2008a; Gregor et al., 2009) and in the stromal vascular fraction (SVF) of adipose tissue where ATMs are enriched (Shan et al., 2017). Recent studies have implicated ER stress as an early event of nutrient excess in the development of insulin resistance (Boden et al., 2008b; Cnop et al., 2012; Kawasaki et al., 2012; Ozcan et al., 2004). Accordingly, targeting ER stress/IRE1α has been proposed as a direction for the improvement of insulin resistance in obesity and diabetes (Hetz *et al.*, 2013; Marciniak et al., 2021)

However, to this far, the exact role of IRE1α on the adipose function and remodeling remains inconclusive. For example, adipocyte-specific knockout of IRE1α was shown to promote brown adipose tissue (BAT) activation and browning of white adipose tissue (WAT) and alleviate diet-induced obesity and insulin resistance by suppressing its RNase-mediated degradation of the mRNA of thermogenic gene PGC1α and hence elevating UCP1 level (Chen et al., 2022). On the other hand, other studies reported that the IRE1α-XBP1 pathway is required for the transcriptional induction of UCP1 in brown adipocyte in vitro (Asada et al., 2015) and is indispensable for proper adipogenesis (Sha et al., 2009). Additionally, inhibiting IRE1α kinase activity was found to be sufficient to block the inflammation-induced lipolysis in adipocytes (Foley *et al.*, 2021), which is in contrast with the observation that adipocyte deletion of IRE1α promotes β3-AR agonist-stimulated WAT lipolysis as reported (Chen *et al.*, 2022).

The function of IRE1α on adipose tissue remodeling and insulin resistance has also been shown throughn its activity in ATMs. Deletion of IRE1α in myeloid lineage including macrophage was recently shown to prevent mice against diet-induced obesity and insulin resistance (Shan *et al.*, 2017). The IRE1α deletion was reported to achieve

this by reversing the obesity-induced M1/M2 polarization (Shan *et al.*, 2017), leading to the augmented M2 population in adipose tissue that induces BAT activation and WAT remodeling through the synthesis and action of catecholamines (Nguyen et al., 2011; Shan *et al.*, 2017). However, it was recently reported that the alternatively activated M2 macrophages do not synthesize catecholamines or contribute to adipose tissue adaptive thermogenesis (Fischer et al., 2017). Moreover, as mentioned above, the obesity-associated ATMs were recently shown to do not undergo the classical M1/M2 switch but to adopt a metabolic activation state (Hill *et al.*, 2018; Jaitin *et al.*, 2019; Kratz *et al.*, 2014; Xu *et al.*, 2013). It is therefore unclear what changes in the ATM under IRE1α deletion is accountable for the protection against obesity and insulin resistance as observed in the myeloid-specific IRE1α knockout model (Shan *et al.*, 2017). It is unknown whether IRE1α inhibition has any effect on the obesity-induced metabolically activated ATM population.

In this study, we used a pharmacological inhibitor of IRE1α STF-083010 (STF) to investigate the effect of IRE1α inhibition on insulin resistance and obesity in the adult mice. We observed that STF treatment improves insulin sensitivity and protects against weight gain in diet-induced obesity (DIO) mice. IRE1α inhibition also reverses the high fat diet (HFD)-induced whitening of BAT and WAT remodeling and increases thermogenesis. Notably, STF treatment suppressed the M2 ATM subpopulation in the DIO mice. Our studies also showed that IRE1α inhibition diminishes the obesity-elicited pro-inflammatory ATM subpopulations including the newly identified $CD9^+$ ATMs and adipose inflammation which is known to suppress thermogenesis (Goto et al., 2016; Sakamoto et al., 2016; Sakamoto et al., 2013). In all, our study provides new insights

into the mechanisms by which IRE1α inhibition protects against obesity and insulin resistance and serves as a foundation for targeting IRE1α as a therapeutic means in the treatment of obesity and insulin resistance.

2. Materials and Methods.

Animal Studies

C57BL/6J mice were obtained from Jackson laboratory (Bar Harbor, ME). Mice were kept in an animal facility with a 12 h light/dark cycle and temperature of 22 °C. All animals had access to diet and water ad libitum. All procedures involving animals were approved by the Institutional Animal Care and Use Committee of the University of Oklahoma Health Science Center. All experiments were performed with age-matched mice. The C57BL/6J male mice were fed a high-fat diet (HFD) (60% kcal fat, Bio-Serv, NJ, USA) at the age of 5-6 weeks. At the 8-week HFD feeding, mice were randomly divided into two groups and were administered with either vehicle (10% DMSO) or STF (10 mg/kg body weight in 10% DMSO) once daily through the route of intraperitoneal injection. Blood glucose levels were measured using the OneTouch Ultra2 glucometer after fasting for 6 h. Body weights were measured weekly.

Glucose tolerance test and insulin tolerance test

Intraperitoneal glucose tolerance test (ipGTT) was performed after 16-h overnight fasting. Blood glucose levels were measured at 0, 15-, 30-, 60-, and 120-minutes glucometer (OneTouch Ultra 2 Meter) after an intraperitoneal administration of glucose at dose of 1.5 g/kg body weight. Intraperitoneal insulin tolerance test (ipITT) was

performed after 6 hours fasting. Blood glucose levels were measured at 0, 15, 30, 60, and 120 minutes after an intraperitoneal administration of human insulin at dose of 1.2 IU/kg body weight.

Biochemical analysis

Fasting serum insulin (ALPCO, NH, USA), serum cholesterol TG (Cayman Chem., MI, USA) and FFAs (Bioassay system, CA, USA) were determined by ELISA.

Body composition assessment:

Body lean and fat composition and total body weight were determined by EchoMRI test.

Indirect calorimetry measurements:

The mice were individually housed in chambers of a Promethion Core Monitoring system (Sable Systems, Las Vegas, NV, USA). After a 1-day acclimation period, their oxygen consumption and carbon dioxide production were measured for the next three consecutive days. The respiratory exchange ratio and energy expenditure were calculated using standard equations.

Adipose stromal vascular fraction (SVF) isolation and flow cytometry

Mice were sacrificed and the epididymal visceral white adipose tissue (eWAT) was immediately washed by phosphate-buffered saline (PBS). The tissue was placed in 10-cm petri dish and excised into tiny bits with scissors at room temperature. Transfer the fine chopped tissue pieces in 10 mL plain DMEM containing Collagenase P (0.45

mg/mL) in 50 mL tubes. Keep the tubes in 37 ºC incubator shaker at a speed of 200 rpm for 30-40 minutes. Add 5 mL of media containing FBS to each tube and pipette well and spin at 700 g rcf for 10 minutes at 4˚C. Remove gently all the supernatants, and the remaining pellet is stromal vascular fraction (reddish brown –containing RBC).

For flow cytometry, cells were resuspended in sterile FACS buffer, then filter through 70 μm strainer and centrifuge at 1000 rpm at 4˚C for 5 minutes. Resuspend the pellet in 2 mL of 1X RBC lysis buffer solution (Sigma) and incubated on ice for 2-3 min. Add 10 mL of PBS and spin the cells at 1100 rpm for 5 minutes. The resulting cell suspension was incubated with Fc Block (BD Biosciences) prior to staining with conjugated antibodies for 20 min at 4˚C followed by 2 washes in FACS buffer. Samples were stained using the following antibodies: PerCP-conjugated anti-mouse CD45, FITC-conjugated anti-mouse F4/80, PE-conjugated anti-mouse/human CD11b, BV421-conjugated anti-mouse CD11c, Alexa Fluor 700-conjugated anti-mouse CD206, PE Dazzle594-conjugated anti-mouse CD9, APC-conjugated Trem2, PE-Cy7-conjugated anti-mouse CD63, purchased from Biolegend. Cells were analyzed using Aurora Spectral Flow Cytometer (Cytek) and FlowJo software (FlowJo, LLC). Sorting was performed using MoFloXDP (Beckman Coulter). Single cells were sorted into 1.5 mL tube containing 50 µL of DMEM medium. Immediately after sorting, tubes were spun down and removed the medium, snap-frozen on dry ice and stored at −80°C until further processing.

SVF culture and treatment in vitro

Freshly isolated SVF portions were cultured in RPMI 1640, supplemented with 10% FBS and 1% penicillin/streptomycin (PS) (RPMI/FBS/PS). 2 h after seeding for a density

at $2x10^6$ cells/10 cm-dish, SVF cells were treated with 0.01% DMSO control or 30 μM STF for 20 h. Cells were collected and labeled with the antibodies as above followed by FACS analysis or sorting.

Histology and immunohistochemistry

Adipose tissue and liver were dissected and immediately fixed in 4% paraformaldehyde (Sigma–Aldrich), paraffin embedded, and stained with hematoxylin and eosin. For Immunofluorescence staining, the eWAT and iWAT paraffin sections were incubated with primary antibody F4/80 (Cat#:70076, Cell Signaling Technology), CD9 (Cat#:ab223052, Abcam), Trem2 (Cat#: MAB17291, R&D Systems) UCP1(Cat#:ab10983, Abcam) overnight at 4 °C after deparaffinization. The slides were washed thrice with PBS with 0.2% Triton and then incubated in Alexa Fluor 488-, 555-, and 647- conjugated secondary antibodies (Jackson ImmunoResearch, PA), DAPI (0.5 mg/mL) for 1.5 h at room temperature. Tissue sections were imaged on the Olympus Fluoview 1000 laser-scanning confocal microscope (Center Valley, PA) and quantified with Image-J histogram software.

RNA extraction and RT-PCR:

Total RNA (2 µg) was isolated from tissues or cells using TRIzol reagents (Life Technologies) or total RNA (0.1-0.5 µg) from sorted cells using E.Z.N.A. total RNA kit (Omega Bio-Tek, Norcross, GA) isolated and reverse transcribed using oligo d(T) primers (New England Biosystems) and SuperScript IV reverse transcription kit (Applied Biosystems, Foster City, CA). qPCR was performed in a CFX96 Touch Real-Time PCR

detection system using SYBR Green mix (Applied Biosystems, Foster City, CA). The amplification program was as follows: initial denaturation at 95°C for 15 min, followed by 40 cycles of 95°C for 15 s, 60°C for 1 min, and 40°C for 30 s. Relative mRNA expression was determined by the ΔΔCt method normalized to TBP mRNA. The sequences of primers used in this study are found in Supplemental Table 3. Regular RT-PCR was performed and the products were resolved by agarose gel electrophoresis. The unspliced and spliced XBP1 mRNA levels were quantified using ImageJ software (National Institutes of Health, Bethesda, MD).

Western blotting

Proteins were extracted with RIPA buffer containing protease and phosphatase inhibitors (Thermo) and then centrifuged for 10 min at 10,000 g. Total protein concentration in the cell lysate was determined by BCA. Samples of ~ 30 μg protein prepared with (reducing) 5% β-mercaptoethanol were separated on a 4-12% Bis-Tris NuPAGE gels (Invitrogen) and transferred to polyvinylidene-fluoride membrane for 1 h at 4°C at 40 V. The membrane was blocked in TBS (10 mm Tris-HCl, pH 7.4, 150 mm NaCl) containing 3% BSA for 1 h at room temperature and was probed with primary antibodies followed by the appropriate HRP-conjugated secondary antibodies (1:5000; Santa Cruz Biotechnology, CA, USA). The primary antibodies were: Phospho-Akt (Ser473) (4060S, Cell Signaling Technology), Akt (pan) (4685S, Cell Signaling Technology), GAPDH (sc-365062, Santa Cruz Biotechnology).

Statistical Analysis

All data are presented as the mean ± SEM of the indicated number of replicates. Data were analyzed using the unpaired two-tailed Student's t-test or ANOVA with multiple comparisons (Prism) and $p<0.05$ was considered statistically significant. For energy expenditure experiments, the data was analyzed for group effect (ANOVA) along with the mass and interaction effects as necessary (generalized linear model, GLM) (Mina et al., 2018).

Supplemental Table 3

Primers used in this work

Gene	Forward Primer	Reverse Primer

GAPDH	AAAGACTGGAGCCCCACACTCTAC	ATCCCGTATTTCACCTCTGCTTC
XBP1s	GAG TCC GCA GCA GGT	GTG TCA GAG TCC ATG
XBP1u	CGCAGACTGCTCGAGATAGA	CCACAAGGCCGTGAGTTTTC
Chop	GCAGCGACAGAGCCAGAATA	CAAGGTGAAAGGCAGGGACT
Bip	GTGTGTGAGACCAGAACCGT	GCAGTCAGGCAGGAGTCTTA
EDEM1	CAAGTGTGGGTACGCCACG	AAAGAAGCTCTCCATCCGGTC
Blos1	CAAGGAGCTGCAGGAGAAGA	CCAGGAGGGTGAAGTAAGAGG
Col61a	TGCTCAACATGAAGCAGACC	TTGAGGGAGAAAGCTCTGGA
ATF4	CCTATAAAGGCTTGCGGCCA	GCTGGATTTCGTGAAGAGCG
UCP1	CACCTTCCCCCTGGACACT	CCCTAGGACACCTTTATACCT
Prdm16	AGGAGGAGGAGAGAGATTCCG	GTCCGGGTCAGGTTCATACAT
PGC1-α	CCCTGCCATTGTTAAGACC	TGCTGCTGTTCCTGTTTTC
Cidea	ATCACAACTGGCCTGGTTACG	TACTACCCGGTGTCCATTTCT
Cox5b	TGCTACCTCCAAAGGCAGCTTC	CATCGCTGACTCTCGCCTTTGT
Cox7a1	CAGCGTCATGGTCAGTCTGT	AGAAAACCGTGTGGCAGAGA
Cox8b	GAACCATGAAGCCAACGACT	GCGAAGTTCACAGTGGTTCC
Ppara	TTCCCTGTGAACTGACGTTT	CCACCATGTTGGATGGATGTG
DIO2	AGAGTGGAGGCGCATGCT	GGCATCTAGGAGGAAGCTGTT
β1AR	CCGAAAGCAGGTGAATGCAA	AGCCAGTAAGCCATACTAAGCCACA
β2AR	CATTGATGTGTTGTGCGTCA	ACTCGGGCCTTATTCTTGGT
β3AR	CCTTCCGTCGTCTTCTGTGT	AGCCATCAAACCTGTTGAGC
TNF-α	CTGAACTTCGGGGTGATCGG	CTACGACGTGGGCTACAGG
IL-1β	TGCCACCTTTTGACAGTGATG	TGATGTGCTGCTGCGAGATT
IL-6	CACTTCACAAGTCGGAGGCT	CTGCAAGTGCATCATCGTTGT
MCP-1	AGGTCCCTGTCATGCTTCTG	TCTCCAGCCTACTCATTGGGA

Mgl1	CAGATCTGGGGCCGTCAAG	GGGAGGAAATGCATCTGGGT
IL-10	AGGCGCTGTCATCGATTTCT	ATGGCCTTGTAGACACCTTGG
F4/80	TCTGCTTCTGTACAGCCACG	CCTCAGAACCCACAGTGTCC
CD68	TGTTCAGCTCCAAGCCCAAA	GTACCGTCACAACCTCCCTG
Abca1	TAGCAGCACCGTGTCTTGTC	GCGTGTCACTTTCATGGTCG
CD36	TCCAGCCAATGCCTTTGC	TGGAGATTACTTTTCAGTGCAGAA
Plin2	TCTGCGGCCATGACAAGTG	GCAGGCATAGGTATTGGCAAC
ATP6V1B2	AGCCTCGTCTCACCTACAAGA	CTCAGCGTATCTGGGAAACTT
ATP6V0D2	AGCCAGCCTAACTCAGC	GCTTCTTCCTCATCTCCGTGTC
Lamp2	ATGTGCCTCTCTCCGGTTAAA	GCAAGTACCCTTTGAATCTGTCA
Lipa	GGAAACAGCAGAGGAAACACCT	CACGGGAGCCAAGACTAAAAC
Fabp4	GGGGCCAGGCTTCTATTCC	GGAGCTGGGTTAGGTATGGG
Fabp5	ACGGCTTTGAGGAGTACATGA	CTCGGTTTTGACCGTGATG
Ctsb	CAATGGCCGTTGAATGCACA	TGGTGTATGGTAAGCAGTG
Trem2	AAAGCTAGCATGGAACCTCTC	TTGAATTCGAGCTCTCTAGACGT
CD9	TGGGGCTATACCCACAAGGA	GCTTTGAGTGTTTCCCGCTG
PEPCK	TGAAAGGCCGCACCATGTAT	GGGCGAGTCTGTCAGTTCAA
G6P	ATCCGGGGCATCTACAATG	TGGCAAAGGGTGTAGTGTCA
ACC	GCCTCTTCCTGACAAACGAG	TGACTGCCGAAACATCTCTG
SCD-1	GAGGCCTGTACGGGATCA	GCCCAGTCGTACACGTCA
Fasn	GCTGGCATTCGTGATGGAGTCGT	AGGCCACCAGTGATGATGTAACTCT

RESULTS

IRE1α RNase inhibition ameliorates insulin resistance in diet-induced obese mice

We first examined whether the ER stress response/UPR pathway was altered in the adipose tissues of obese animals. In C57B/6J mice fed high fat diet for 14 weeks, we observed that the mRNA levels of genes representing all three branches of UPR (spliced Xbp1 (Xbp1s) for IRE1α branch, ATF4 and CHOP for PERK branch, and EDEM1 and Bip for ATF6 branch) were up-regulated in both epididymal white adipose tissues (eWAT) (Fig. 1A) and inguinal white adipose tissue (iWAT) (Fig. S1A). As IRE1α activation is associated with the IRE1-dependent decay of mRNA (RIDD) activity in which IRE1 cleaves mRNAs, we analyzed the mRNA levels of two RIDD targets *Blos1* and *Col6a1* by qRT-PCR. We observed that *Blos1* and *Col6a1* mRNA levels were decreased in the eWAT (Fig. 1B) while *Col6a1* mRNA level was also down-regulated in the iWAT (Fig. S1B) of HFD-fed mice. These results suggest the over-nutrition/obesity triggers ER stress and IRE1α activity in adipose tissue.

We then asked whether IRE1α activation contributes to obesity-induced insulin resistance and importantly whether pharmacological inhibition of IRE1α can reverse the pre-existing obesity-induced insulin resistance. We used a specific inhibitor STF-083010 (STF) of IRE1α RNase to treat diet-induced obesity (DIO) mice with established insulin resistance. Male C57B/6J mice fed on HFD for 8 weeks gained significant glucose intolerance (Fig. S1C) and were treated with STF at 10 mg/kg of BW once daily for 4 weeks via IP injection, a dose previously shown to significantly inhibits IRE1α RNase activity in vivo (Herlea-Pana et al., 2021; Papandreou et al., 2011; Tufanli et al., 2017), while still on HFD. We observed that STF treatment improved glucose tolerance with lower peak glucose level and decreased AOC (area of the curve) in response to a bolus of exogenous glucose compared to their vehicle-treated counterpart (Fig. 1C-C'). STF

treatment significantly improved insulin sensitivity in DIO mice (Fig. 1D-D'). We also observed markedly decreased resting and glucose-stimulated plasma levels of insulin in DIO mice treated with STF (Fig. 1E), indicative of increased insulin sensitivity in the STF-treated mice. To investigate whether the increased insulin sensitivity by STF is reflected in insulin signaling, we examined the phosphorylation status of Akt, an effector of insulin signaling pathway, in the adipose tissue. Contrary to the significant enhancement in the insulin-stimulated Akt phosphorylation at Ser473 observed in the epididymal white adipose tissue (eWAT) of non-HFD lean animals, the insulin-stimulated Akt phosphorylation at Ser473 was blunted in the eWAT of DIO mice. However, STF treatment significantly reversed the insulin-stimulated Akt phosphorylation (Fig. 1F-F'). Collectively, these data indicate that STF improves insulin sensitivity and glucose control under HFD.

To investigate whether the STF amelioration of insulin resistance and obesity reflects on its inhibition of IRE1α activity in adipose tissue, we examined the status of IRE1α-mediated *Xbp1* mRNA splicing in WAT from STF-treated DIO mice and observed that as assessed by RT-PCR followed by electrophoretic separation, the level of spliced *Xbp1* (*XBP1-s*) mRNA was significantly reduced in both eWAT (Fig. 1G-G') and iWAT (Fig. S1D-D') from STF-treated animals relative to vehicle group. Moreover, the mRNA levels of XBP1 target genes *Bip* and *EDEM1* were highly suppressed in both eWAT and iWAT from STF-treated mice (Fig. 1H and S1E). Interestingly, we also observed the decrease in the mRNA levels of *ATF4* and *CHOP*, key components of the PERK pathway in eWAT and iWAT of STF-treated DIO mice (Fig. 1H and S1E). The effect of STF treatment on PERK pathway in the adipose tissue probably reflects the positive

feedback loops among the branches of UPR under in vivo conditions as previously reported (Kapuy et al., 2020; Márton et al., 2017; Tsuru et al., 2013).

STF protects against diet-induced obesity and obesity-associate morbidities.

We observed that while vehicle-treated mice continued to gain weight on HFD, 4-week STF treatment slightly decreased the body weight (Fig. 2A and S2A), with no apparent food intake difference between the vehicle and STF groups (Fig. S2B). Body composition analysis using EchoMRI also revealed that STF treatment resulted in a significant decrease in the fat mass but without significant changes in the lean mass (Fig. 2B) in the HFD-fed mice. We next analyzed the size of adipocytes in WAT sections and observed that adipocytes were significantly smaller from STF-treated DIO mice than that of vehicle-treated ones (Fig. 2C, 2F) as shown in both average diameters (Fig. 2D. 2G) and frequencies in large adipocytes (Fig. 2E, 2H) in both eWAT and inguinal WAT (iWAT). The average area of adipocytes was similarly significantly shrunk in the eWAT (Fig. S2C) and iWAT (Fig. S2D) of DIO mice treated with STF relative to vehicle treatment. In addition, there was a significant reduction in lipid droplets in the brown adipose tissue (BAT) from STF-treated DIO mice (Fig. 2I).

A common comorbidity of obesity and insulin resistance is nonalcoholic fatty liver disease (NAFLD) (Khan et al., 2019). We therefore investigated the potential effects of STF on liver steatosis in obesity. First, we examined the liver histology in haematoxylin and eosin-(H.E.) stained sections. We observed the presence of numerous lipid droplets in the liver, a hallmark of live steatosis, in the vehicle-treated DIO mice compared to that in the BL/6 mice fed normal chow (Fig. 3A). Strikingly, STF treatment markedly reduced

the number of the lipid droplets in the liver of DIO mice compared to vehicle treatment (Fig. 3A). We next examined the expression of genes involved in lipogenesis in the liver of the STF- and vehicle-treated DIO mice and found that the lipogenic genes FASN, stearoly-coA desaturase-1 (*SCD-1*), and acetyl coA-carboxylase (*ACC*) were down-regulated in the liver of STF-treated DIO mice compared to vehicle-treated mice (Fig. 3B). Furthermore, because NAFLD is associated with an impaired suppression of hepatic glucose output (Marchesini et al., 2001), we assessed the expression of genes involved in gluconeogenesis, including glucose-6-phosphatase catalytic subunit (*G6PC*) and *PEPCK*. We found that the expression level of G6PC in the liver from STF-treated DIO mice was also significantly decreased compared to that of vehicle-treated ones while there was no effect on PEPCK expression (Fig. 3C). NAFLD is also characterized by excessive inflammation, in particular macrophage accumulation, in addition to lipid deposition (Lefere and Tacke, 2019). We therefore investigated the effect of STF on macrophage population in the obese liver and observed that STF treatment suppressed the macrophage accumulation of DIO mice, as marked by the F4/80 immunofluorescent staining (Fig. 3D-E). Furthermore, obesity is tightly associated with dyslipidemia. We therefore examined the effect of STF on dyslipidemia and observed that STF treatment decreased the plasma levels of triglyceride, free fatty acid (FFA), and total cholesterol (Fig. 3F-H).

STF treatment promotes thermogenesis and energy expenditure.

The observation that STF treatment protects against HFD-induced obesity (Fig. 2A) suggests an increase in energy expenditure (EE) in these mice. We therefore

investigated this in DIO mice treated with STF. We observed that average oxygen consumption (VO_2) was higher in DIO mice treated with STF than with vehicle, using indirect calorimetry (Figs. 4A-B and S2E-E'). Similarly, the average carbon dioxide production (VCO_2) was significantly increased in STF -treated DIO mice (Figs. 4C-D and S2F-F'). As a result, we found that STF treatment moderately but significantly increased mean (EE) compared to vehicle treatment (Figs. 4E-F and S2G-G'), without alterations in respiratory exchange ratio (RER) value or physical activities (Fig. 4G-H).

To ask whether the energy expenditure increase by STF is attributable to thermogenic heat production, we investigated the effect of STF treatment on the activation status of brown adipose tissue (BAT) in DIO animals. BAT is an organ specialized for energy expenditure through the action of mitochondrial uncoupling protein 1 (UCP1). During obesity, lipid-droplet content is increased in BAT (whitening of BAT), which impairs its ability to dissipate the energy. We observed that STF treatment reversed the whitening of BAT, as reflected in much less lipid droplet intensity in BAT, in DIO mice compared to vehicle treatment (Fig. 2I). Immunofluorescent staining showed the elevated staining intensity of UCP1 protein in BAT per unit area in DIO mice compared to vehicle treatment (Fig. 4I-K). Furthermore, STF-treated mice showed increased expression of genes involved in thermogenic and mitochondrial functions, including Prdm16, UCP1, Cidea, Ppara, DIO2, Cox 5b, and Ppargc1a (PGC1α), in BAT (Fig. 4L). These data thereby suggest that STF promotes BAT activation. Induction of beige fat in the WAT also plays important role in the adaptive thermogenesis and energy expenditure (Kajimura et al., 2015). We therefore examined the effect of STF on the status of beiging activation in the WAT. The immune-signal intensity of UCP1 protein was

markedly increased in the eWAT (Fig. 4M and S3A) and iWAT (Fig. S3B-C) of DIO mice treated with STF. In addition, the expression of thermogenic genes was significantly increased in both eWAT and iWAT of DIO mice subjected to STF treatment compared to vehicle (Fig. 4N and Fig. S3D). These results suggest the involvement of beige fat activation in thermogenesis and energy expenditure in STF-treated mice. Moreover, we also investigated the effect of STF on the expression of β-adrenoceptors, which play important role in adaptive thermogenesis in response to cold stimulation, on adipose tissues and observed that STF treatment elevated the levels of both β2-adrenoceptor (β2AR) and β3AR in BAT (Fig. 4O) and the levels of β3AR in iWAT and eWAT (Fig. S3E-F).

Effect of STF treatment on obesity-associated macrophage activation

Since adipose tissue macrophage (ATM) accumulation plays important role in contributing to insulin resistance and obesity (Lumeng *et al.*, 2007; Xu *et al.*, 2003), we investigate whether STF treatment impacts ATM accumulation in DIO mice as IRE1α activity was observed to be heightened in obese macrophages (Shan *et al.*, 2017). During obesity, the expansion of adipose tissues accompanies the recruitment and accumulation of macrophages in the adipose tissue, and crown-like structures (CLS) are formed upon the infiltration and residence of macrophages around dead adipocytes in the adipose tissues (Cinti et al., 2005). As shown in Figs. 2C and 5A, the area of CLS was drastically reduced in the eWAT of DIO mice treated with STF relative to vehicle-treated mice, although CLS area showed no significant difference in iWAT between vehicle and STF groups (Fig. S4A). Immunofluorescent staining of F4/80, a pan-macrophage marker, was drastically increased in the eWAT under HFD, but was

reversed in STF-treated mice (Fig. 5B-C). Moreover, we examined the expression levels of pan-macrophage marker genes (CD68 and F4/80) and found that STF treatment significantly alleviated the mRNA levels of CD68 and F4/80 in the stromal vascular fraction (SVF where immune cells reside) of the eWAT (Fig. 5D). Expectedly, STF treatment also inhibited the splicing of IRE1α target XBP1 mRNA in the eWAT SVF (Fig. S4B-D). Next, we used flow cytometry to analyze the changes of ATMs by STF treatment under HFD. We observed that the percentage of macrophage population (double positive for F4/80 and CD11b markers ($F4/80^{+}CD11b^{+}$)) did not alter substantially in the SVF fraction isolated from eWAT under HFD compared to normal chow (Figs. 5E and S5A); however, given the HFD-induced expansion of the eWAT, the total number of $F4/80^{+}CD11b^{+}$ macrophages has increased drastically by 49.6 fold: 0.29 ± 0.25 $x10^{5}$ (normal chow) vs. 1.43 ± 0.086 $x10^{6}$ (14-week HFD) cells/eWAT fat pad/mouse (P=0.0041) (Table 1a). The density of $F4/80^{+}CD11b^{+}$ macrophage population in eWAT also increased under HFD by 12.5 fold after normalizing the total number of macrophages to fat pad weight (0.62 ± 0.45 $x10^{5}$ (normal chow) vs. 0.77 ± 0.015 $x10^{6}$ cells (14-week HFD)/g of eWAT/mouse, P=0.0045, Table 1a). Excitingly, STF treatment significantly lessened the HFD-induced increases in the percentage, total number, and density of ATMs by 37.4%, 46%, and 54%, respectively (Figs. 5E and S5A and Table 1a). These results indicate that STF suppresses macrophage accumulation in the adipose tissue.

It was previously reported that macrophages that accumulated in adipose tissues undergo a “phenotypic switch” from an anti-inflammatory M2 (alternatively activated) phenotype to a proinflammatory M1 (classically activated) state, a process believed to

be critical for the development of systemic insulin resistance (Lumeng *et al.*, 2007). We therefore investigated the effect of STF treatment on such an ATM switch. We observed that under HFD, the percentage ((14.59% (ND) vs. 52.95% (HFD), P=0.007, Figs. 5F and S5A, Table 1b), total number/eWAT/mouse (0.25 ± 0.16 x10^4 (ND) vs. 0.75 ± 0.11 x10^6 (HFD), 299.58-fold, P<0.0001, Table 1b), and density/g of eWAT/mouse (0.59 ± 0.23 x 10^4 (ND) vs. 4.11 ± 0.96 x 10^5 (HFD), 70-fold, P=0.0018, Table 1b) of F4/80$^+$CD11b$^+$CD11c$^+$ triple positive cells, which are typically characterized as the classical "M1-like" adipose tissue macrophages, were markedly increased in the eWAT. Unexpectedly, we found that the bulk majority of these CD11c$^+$ ATMs were also positive for CD206, a marker thought for M2 macrophages, in the eWAT under HFD (Fig. S5B), and that approximately half the population is positive for both CD11c and CD206 in DIO ATMs whereas there are only 8.55% CD11c$^+$CD206$^+$ ATMs under ND when gated against CD11c and CD206 (Figs. 5G and S5A), suggesting the enrichment of a mixed M1/M2 phenotype, which is consistent with recent reports (Shaul et al., 2010; Sica and Mantovani, 2012; Wentworth et al., 2010). Moreover, we found that the total number and density of CD11c$^+$CD206$^+$ ATMs increased by 337- and 75-fold respectively under HFD (Table 1c), a greater increase than those of CD11C-postive alone (CD11c$^+$CD206$^-$) ATMs under HFD (Table S1a). On the other hand, for CD206$^+$CD11c$^-$ ATM subpopulation, a presumed M2-like ATM subpopulation which accounted for the majority of ATMs under ND as expected (Fig. 5G and Table 1d), HFD drove the increase in the total cell number and density of this population by over 16- and 4-fold respectively despite the diminished percentage given the huge expansion of total ATMs (Table 1d), although to a lesser degree than that for CD11c$^+$CD206$^+$ or CD11c$^+$CD206$^-$

macrophages (Tables 1c and S1a). Moreover, $CD206^{-}CD11c^{-}$ ATM subpopulation also exhibited a trend similar to that of $CD206^{+}CD11c^{-}$ ATMs (Table S1b). Our findings confirm the notion that ATMs do not follow the classic M2 to M1 switch (Hill *et al.*, 2018; Kratz *et al.*, 2014; Xu *et al.*, 2013).

It has been reported that the germline deletion of IRE1α in myeloid lineage reverses the switch in M1/M2 polarization with the increase in M2 population to induce BAT activation and WAT remodeling and protect mice against diet-induced obesity (Shan *et al.*, 2017). However, in light of increasing evidence from others (Hill *et al.*, 2018; Kratz *et al.*, 2014; Xu *et al.*, 2013) and our current findings that do not support a HFD-triggered classical M1/M2 polarization, we sought to interrogate the effect of IRE1α inhibition on ATM subpopulations, which by far is poorly understood. In DIO mice treated with STF for 4 weeks, we found that consistent with the overall reduction of ATM population (Fig. 5E, Table 1a), the percentage, total number, and density of the posited "M1-like" $F4/80^{+}CD11b^{+}CD11c^{+}$ triple positive cells were substantially diminished in the SVF of eWAT (Fig. 5F and S5A, Table 1b), but to an even greater extent than the overall ATM population. The trend in the reduction of $F4/80^{+}CD11b^{+}CD11c^{+}$ ATMs by STF remains similar regardless of whether $CD206^{+}$ was positive ($F4/80^{+}CD11b^{+}CD11c^{+}CD206^{+}$) or negative ($F4/80^{+}CD11b^{+}CD11c^{+}CD206^{-}$) (Fig. 5G, Tables 1c and S1a). In addition, the total number and density of M2-like $CD206^{+}CD11c^{-}$ ATMs were also significantly reduced in the SVF of eWAT of STF-treated DIO animals (Table 1d), but to a lesser degree than $CD11c^{+}$ ATMs. In contrast, STF treatment even slightly increased the total number and density of the CD206 CD11c double-negative ATMs ($CD206^{-}CD11c^{-}$

F4/80^{+}CD11b^{+}) or non-macrophage (F4/80^{-}CD11b^{-}) populations (Tables S1b and S1c), although none of them reaching statistically significance.

As the “M1-like” CD11c^{+} and M1/M2 mixed ATMs were reported to be associated with pro-inflammation (Shaul *et al.*, 2010; Wentworth *et al.*, 2010), we examined the mRNA levels of proinflammatory cytokine genes —*TNFα*, *IL1b*, *IL-6*, and *monocyte chemoattractant protein-1* (*mcp-1*)— and found that they were down-regulated in the SVFs of eWAT from STF-treated DIO mice compared to vehicle-treated counterparts (Fig. 5H), which correlates with our observed decreased populations of “M1-like” CD11c^{+} and M1/M2 mixed ATMs in the STF-treated DIO animals (Fig. 5E-F). Similarly, STF treatment also inhibited the mRNA levels of these cytokine genes in the SVFs of iWAT (Fig. S5C). Furthermore, in CD11c^{+} ATMs (F4/80^{+}CD11b^{+}CD11c^{+}) sorted from the eWAT SVFs of DIO mice, which expectedly expressed higher mRNA levels of *TNFα*, *IL1b*, and *Mcp-1* than CD11c^{-} ATMs (Fig. 5I), STF treatment remarkably reduced the expression levels of *TNFα*, *IL1b*, and *Mcp-1* (Fig. 5J). STF inhibited the IRE1α RNase activity in these cells as reflected by the diminished XBP1-s mRNA levels (Fig. S5D). These results reveal that STF treatment suppresses the accumulation of ATM and inflammation without augmenting (suppressing instead) M2-like ATMs.

Metabolically active ATMs are suppressed in DIO mice by STF treatment

Recent studies have shown that instead of the classical proinflammatory M1 polarization, obesity drives the expansion of metabolically active heterogeneous ATM populations. These metabolically active ATMs possess heightened lysosome and lipid

483 metabolism (Coats *et al.*, 2017; Kratz *et al.*, 2014; Xu *et al.*, 2013), express cell surface
484 markers CD9 or Trem2 at a higher frequency, and are pro-inflammatory (Hill *et al.*, 2018;
485 Jaitin *et al.*, 2019). These studies reported that the $CD9^+$ macrophages have high
486 amounts of intracellular lipid in lysosome-like structures, express genes related to
487 lysosomal-dependent lipid metabolism (Hill *et al.*, 2018) and represent the majority of
488 total adipose tissue macrophages in obesity (Jaitin *et al.*, 2019). Given our findings on
489 the significant inhibitory effect of STF on ATM accumulation and inflammation, we
490 therefore investigated whether STF impacts these alterations in the adipose tissues of
491 DIO mice. We first determined the effect of STF treatment on the metabolic activation of
492 ATMs. Proteins involved in lipid metabolism including ABCA1, CD36, and PLIN2 were
493 reported to be specifically up-regulated in metabolically active macrophages in obesity
494 (Kratz *et al.*, 2014). We observed that the mRNA levels of *ABCA1*, *CD36*, and *PLIN2*
495 were elevated in the SVF portion of the eWAT in DIO mice compared to their normal
496 diet counterparts, but STF treatment significantly suppressed the up-regulation of these
497 genes (Fig. 6A). Moreover, genes involved in lysosomal biogenesis and phagocytosis
498 including *ATP6V1B2*, *ATP6V0D2*, *LIPA,* and *LAMP2* were also reported to be induced
499 in the ATMs in obesity (Coats *et al.*, 2017; Xu *et al.*, 2013). We therefore examined the
500 effect of STF on the mRNA levels of *ATP6V1B2*, *ATP6V0D2*, *LIPA,* and *LAMP2* and
501 observed that their mRNA levels were elevated in the SVF portion of the eWAT in DIO
502 mice and that STF treatment suppressed the up-regulation of these genes, although the
503 suppression on Lipa does not reach statistical significance (Fig. 6B). In addition,
504 expression levels of other genes known to be involved in lipid metabolism and
505 lysosomal biogenesis, including *Fabp4*, *Fabp5*, and *Stsb1*, were also suppressed by the

treatment of STF (Fig. 6C). Lastly, we also observed a similar trend on the effect of STF treatment in the SVFs of the iWAT (Fig. S6A-B).

We next investigated the effect of STF on the newly identified ATM subpopulations. First we observed that the mRNA levels of *CD9* and *Trem2* were elevated in the SVFs of the eWAT and iWAT in DIO mice relative to age-matched normal chow-fed mice but STF treatment suppressed the up-regulation of these genes (Fig. 6D and S6C)). In addition, immunofluorescent staining of CD9 and Trem2 was drastically increased in the eWAT under HFD (Fig. S6D-E), but was profoundly diminished in STF-treated DIO mice (Fig. 6E-G). Similarly, we observed a similar trend in the effect of STF on the immunofluorescent staining of CD9 and Trem2 in BAT (Fig. S7A) and iWAT (Fig. S7B-C) slides from DIO mice treated with STF or Veh, although without reaching statistical significance. We also noticed that $CD9^+$ and/or $Trem2^+$ macrophage accumulation in iWAT and BAT is significantly less severe than in the eWAT under HFD. We then used flowcytometry to characterize the effect of STF on CD9- or Trem2-expressing ATM subpopulations. We initially examined the HFD-induced changes in these populations. As expected, the percentage (23.25 ± 8.75% (ND) vs. 72.70 ± 2.60% (HFD), P=0.032, Fig. 6H, Table 2a), total number (0.45 ± 0.32 x 10^4 /eWAT/mouse (ND) vs. 1.04 ± 0.026 x $10^{6.}$ /eWAT/mouse (HFD), 228-fold, P=0.00062, Table 2a), and density (1.04 ± 0.51 x 10^4 /g of fat pad (ND) vs. 0.56 ± 0.032 x 10^6 /g of fat pad (HFD), 54-fold, P=0.0034, Table 2a) of the $CD9^+$ ATMs ($F4/80^+CD11b^+CD9^+$) in the eWAT were increased under HFD. It was previously reported that CD63 is enriched in $CD9^+$ ATMs (Jaitin *et al.*, 2019); indeed, we found that up to 98% of $CD9^+$ ATMs also expressed CD63 in HFD-fed mice

(Fig. S6F). As expected, the percentage, total number, and density of $CD9^+CD63^+$ ATMs increased significantly in the eWAT (Fig. S6G and Table S2). Similarly, $Trem2^+$ ATM subpopulation expanded markedly in the percentage, total number/eWAT/mouse, and density (number/g of fat pad/mouse) under HFD (Fig. 6I, Table 2b). In addition, we found that approximately 47% of the $CD9^+$ ATMs ($F4/80^+CD11b^+CD9^+$) express Trem2 while an overwhelming majority (~86.7%) of $Trem2^+$ ATMs ($F4/80^+CD11b^+Trem2^+$) expresses CD9 (Fig. S6H), corroborating a previous finding that $Trem2^+$ expression emerges after $CD9^+$ ATMs over the course of obesity (Jaitin *et al.*, 2019). As expected, double-positive $CD9^+Trem2^+$ ATMs also expanded tremendously under HFD (Fig. 6J, Table 2c). In DIO mice treated with STF, we observed a decrease in the percentages of $CD9^+$, $Trem2^+$, and $CD9^+Trem2^+$ ATMs relative to that of vehicle-treated mice (Figs. 6H-J, Tables 2a-c). Further, STF treatment significantly diminished the total number and density of $CD9^+$, $Trem2^+$, and $CD9^+Trem2^+$ ATM subpopulations all by over 60% (Tables 2a-c).

The CD9-expressing ATM subpopulation under HFD was proposed to be pro-inflammatory (Hill *et al.*, 2018; Jaitin *et al.*, 2019). Indeed, we observed that compared to $CD9^-$ ATMs sorted from the eWAT of DIO mice, the sorted $CD9^+$ ATMs expressed significantly higher mRNA levels of pro-inflammatory genes *TNFα*, *IL1b*, and *Mcp-1* (Fig. 6K). Similarly, the mRNA levels of *TNFα*, *IL1b*, and *Mcp-1* were also heightened in sorted $Trem2^+$ ATMs relative to $Trem2^-$ ATMs (Fig. 6L). Notably, STF treatment of DIO mice markedly reduced the expression levels of *TNFα*, *IL1b*, and *Mcp-1* in $CD9^+$ ATMs sorted from the eWAT (Fig. 6M). A similar trend was obtained in sorted $Trem2^+$ ATMs

from the obese eWAT (Fig. 6N). These results together demonstrated that STF treatment suppresses the subpopulations of metabolically active CD9 and Trem2-positive ATMs and adipose inflammation.

To investigate whether IRE1α inhibition acts on ATMs directly, we examined the effect of STF on the macrophage population and inflammation in SVF cells (freshly isolated from obese eWATs) treated with STF. We observed that STF treatment for 20 hours slightly but statistically significantly diminished the percentage of ATMs (F4/80$^+$CD11b$^+$) (DMSO 56.03% vs. STF 49.30%, p=0.0024) as analyzed by flow cytometry (Fig. 6O). When further gated against Trem2, we observed a trend similar to that for the overall ATMs in that STF treatment moderately but significantly decreased the percentage of Trem2$^+$ ATMs (F4/80$^+$CD11b$^+$Trem2$^+$) (DMSO 68.67% vs. STF 61.93%, p=0.0013) (Fig. 6P). We also observed that STF mildly lessened the percentages of CD9$^+$ ATMs (F4/80$^+$CD11b$^+$CD9$^+$) (DMSO 76.73% vs. STF 74.80%, p=0.013) (Fig. S8A) and of CD11C$^+$ ATMs (F4/80$^+$CD11b$^+$CD11C$^+$) (DMSO 81.23% vs. STF 77.63%, p=0.0040) (Fig. S8B). We next investigated the effect of STF on the expression levels of pro-inflammatory genes in ATMs sorted from STF- or DMSO-treated SVF cells. STF treatment decreased spliced XBP1 mRNA levels (Figs. 6Q, S8C, S8G, S8I), reflecting the inhibition of IRE1α RNase activity, and significantly down-regulated the expression levels of pro-inflammatory genes (*TNFα*, *IL1b*, and *Mcp-1*) in CD9$^+$ ATMs (F4/80$^+$CD11b$^+$CD9$^+$) (Fig. 6R) and in CD11C$^+$ ATMs (F4/80$^+$CD11b$^+$CD11C$^+$) (Fig. 6S), relative to DMSO control-treated counterparts. Similarly, in CD9$^-$ ATMs (F4/80$^+$CD11b$^+$CD9$^-$) or CD11C$^-$ ATMs (F4/80$^+$CD11b$^+$CD11C$^-$) sorted from STF- or

DMSO-treated SVFs, which displayed lower mRNA expression levels of *TNFα*, *IL1b*, and *Mcp-1* compared to their respective $CD9^+$ or $CD11C^+$ counterparts (Fig. S8D-E), STF also down-regulated the mRNA levels of *TNFα*, *IL1b*, and *Mcp-1* (Fig. S8F, S8H). Together, these results indicate that STF acts directly on ATMs to regulate inflammation.

The $CD11c^+$ ATMs are overlapping with but yet distinctly different from metabolically active ATMs in obesity.

One important question on the obesity-associated ATM accumulation is the obscure relationship between the newly-identified $CD9^+$ and $Trem2^+$ ATM populations and the originally identified "M1-like" $CD11c^+$ ATMs (Hill *et al.*, 2018; Wu and Ballantyne, 2020). To investigate this relationship, we analyzed these populations using flow cytometry. First, we asked whether the previously identified $F4/80^+CD11b^+CD11c^+$ triple positive ATMs express signature markers of the newly identified ATM subpopulations (CD9 and/or Trem2) in DIO mice. Our results showed that approximately 80% (91.30 ± 0.40%) of $CD11c^+$ ATMs ($F4/80^+CD11b^+CD11c^+$) express CD9 (Fig. 7A and Table 3a). On the other hand, about 70. 4% of CD11c-negative ATMs ($F4/80^+CD11b^+CD11c^-$) express CD9 (Fig. 7A, Table 3a). We also found that 23.95% of $F4/80^+CD11b^+CD11c^+$ ATMs express $CD9^{-hi}$ while only 3.185% of CD11c-negative ATMs are positive for $CD9^{-hi}$ (Fig. 7A). Similarly, the percentage of cells expressing Trem2 was higher in the $CD11c^+$ ATMs than in $CD11c^-$ ATMs (43.55 ± 8.65% for $CD11c^+$ vs. 24.35 ± 4.05%, albeit not reaching statistical significance (P=0.074), Fig. 7B, and Table 3a). We also observed a higher percentage of the $CD11c^+$ ATMs (30.05 ± 5.55%) expressing both CD9 and

Trem2 than that of CD11c$^-$ ATMs (8.35 ± 1.86%), P=0.066, (Fig. 7C and Table 3a). These results revealed that CD9 and Trem2 are highly enriched but not exclusively expressed in the CD11c$^+$ ATMs under HFD.

In reciprocal studies, we analyzed the distribution of CD11c expression in CD9$^+$ and/or Trem2$^+$ ATMs under HFD. We observed heightened percentages of CD9$^+$, Trem2$^+$, and CD9$^+$Trem2$^+$ ATMs that co-express CD11c (63.25 ± 10.85%, 78.25 ± 12.35%, and 78.65 ± 13.05%, respectively) relative to the CD9$^-$, Trem2$^-$, and CD9$^-$Trem2$^-$ ATMs that co-express CD11c (29.90 ± 9.10%, 49.55 ± 9.85%, or 24.60 ± 5.90%, respectively), in the eWAT of HFD-fed mice (Fig. 7D-F and Table 3b). We also observed that higher percentage of CD9^{hi} ATM subpopulation expresses CD11c than CD9$^+$ ATMs (90.60 ± 1.4% vs. 63.25 ± 10.25%, Fig. 7D). These results showed that while CD11c expression is not exclusively expressed in CD9$^+$, Trem2$^+$, or CD9$^+$Trem2$^+$ ATMs, it is highly enriched in all of these subpopulations. Together, these results reveal that in the eWAT under HFD, the majority of CD11c$^+$ or CD9$^+$ ATMs expresses CD9 or CD11c, respectively. Indeed, up to half (45.45 ± 5.05%) of ATMs in the obese eWAT co-express CD9 and CD11c (F4/80$^+$CD11b$^+$CD9$^+$CD11c$^+$) (Fig. 7G and Table 3c). Notably, similar to its effects on CD9$^+$ or CD11c$^+$ ATMs (Fig. 6H-I), STF treatment substantially decreased the percentage, total number /eWAT/mouse, and density (per gram of fat pad/mouse) of the CD9$^+$CD11c$^+$ ATMs in the eWAT of DIO mice (Fig. 7G, Table 3c). As CD9$^+$ and CD11c$^+$ ATMs were reported to be pro-inflammatory, we next compared the expression levels of proinflammatory genes in these ATM subpopulations from HFD-fed mice and observed that the mRNA levels of *TNFα*, *IL1b*, and *Mcp-1* were all up-

regulated in sorted $CD9^+CD11c^-$, $CD9^-CD11c^+$, and $CD9^+CD11c^+$ ATMs compared to the $CD9^-CD11c^-$ ATMs, with the $CD9^+CD11c^+$ ATMs expressing higher level of Mcp-1 and the $CD9^+CD11c^-$ ATMs expressing lower level of *IL1b* (Fig. 7H), suggesting that these ATM subpopulations are all proinflammatory but yet heterogeneous in nature.

DISCUSSION

In this study, we have shown that the RNase activity of ER stress sensor IRE1α is up-regulated in the adipose tissue of diet-induced obese mice and that the increased IRE1α activity precedes the onset of diabetes in the obese mice. By pharmacologically inhibiting IRE1α using the chemical STF, we found that the inhibition of IRE1α activity is able to reverse HFD-induced insulin resistance and comorbidities, indicating that the increased IRE1α activity is an important contributor to obesity-associated insulin resistance. We showed that STF promotes thermogenesis and energy expenditure and counters diet-induced obesity. Our results also showed that the IRE1α inhibition by STF suppresses the accumulation of proinflammatory ATMs, including previously identified $CD11c^+$ ATMs and the recently identified $CD9^+$ ATMs, and adipose inflammation. Our study also reveals that the $CD11c^+$ ATMs are largely overlapping with but yet non-identical to $CD9^+$ ATMs in the eWAT under HFD.

ER stress and its sensor IRE1α are activated in adipose tissues of obese subjects. IRE1α activation is known to be linked to inflammation via its dual enzymatic activity and its control of transcriptional regulation (Lerner *et al.*, 2012; Martinon *et al.*, 2010; Oslowski *et al.*, 2012) while macrophage activation and inflammation in adipose

tissue is tightly associated with metabolic dysfunction. Targeting ER stress/IRE1α has thus been proposed for its potential in countering obesity and obesity-related metabolic disorders including insulin resistance and type 2 diabetes (Hetz *et al.*, 2013; Marciniak *et al.*, 2021). Indeed, recent studies using tissue-specific deletion of IRE1α in mouse have shown that embryonic IRE1α deletion in macrophage (Shan *et al.*, 2017) and in adipocyte (Chen *et al.*, 2022) prevents diet-induced insulin resistance and obesity. In the present study, we have showed that STF inhibition of IRE1α is capable of reversing existing insulin resistance and obesity and therefore validate the notion of targeting IRE1α inhibition as a potential therapeutic target for the treatment of obesity and related metabolic disorders.

In obese adipose tissue, IRE1α was activated in both adipocytes and ATMs. Acitivated IRE1α was reported to cause its RNase-mediated degradation of PGC1α mRNA and in turn suppression of PGC1α-dependent UCP1 level in adipocytes (Chen *et al.*, 2022). Consistent with this finding, the present study observed that STF treatment decreases the level of IRE1α target RNA s-Xbp1 (Fig. 1G and S1D) and elevates the RNA levels of PGC1α and UCP1 in adipose tissue of DIO mice (Figs. 4L, N). In the adipose tissue macrophage, IRE1α deletion in myeloid lineage using $Ern1^{fl/fl}$;Lyz2-cre was reported to induce the beiging of WAT and protect against diet-induced obesity by augmenting M2 macrophage population through its synthesis and secretion of catecholamine (Shan *et al.*, 2017). It is well established that catecholamines play critical roles on thermogenesis through the activation of β-adrenoceptor signaling in the adipocyte tissue, which is critical for BAT activation and WAT remodeling. Catecholamines are normally synthesized and secreted from sympathetic nerves to

induce adaptive thermogenesis in response to cold stimulation. It was reported that M2 macrophages also produce catecholamines to sustain adaptive thermogenesis (Nguyen *et al.*, 2011). However, this finding was disputed by a recent study showing that M2 macrophages do not synthesize catecholamines (Fischer *et al.*, 2017). Importantly, in contrast to the previous report (Shan *et al.*, 2017), our present study showed that STF treatment does not promote M2 macrophage in the adipose tissue (Fig. 5G and Table 1d), arguing against the possibility that STF inhibition of IRE1α promotes thermogenesis by increasing M2 ATMs. Instead, STF treatment diminishes the M2 ATM population along with the decline of "M1-like" CD11c$^+$ ATMs (Fig. 5F and Table 1b). Notably, STF treatment also significantly diminished the newly identified CD9$^+$, Trem2$^+$, and dual CD9$^+$CD11c$^+$ ATM subpopulations (Fig. 6H-J and Table 2a-c). Like CD11c$^+$ ATMs, CD9$^+$, Trem2$^+$, and dual CD9$^+$CD11c$^+$ ATM express higher levels of pro-inflammatory cytokine genes (Figs. 5K-L and 7I), indicative of their pro-inflammatory nature (Hill *et al.*, 2018; Jaitin *et al.*, 2019). STF treatment accordingly diminishes the expression levels of pro-inflammatory genes in both bulky adipose tissue (Fig. 5H) and sorted ATMs (Figs. 5J and 6M-N). Our in vitro experiments showed that STF treatment directly suppressed the ATM population and the expression of pro-inflammatory genes in these primary ATMs (Figs. 6Q-S and S8). Overall, our study indicates that STF inhibition of IRE1α reverses diet-induced adipose tissue inflammation and proinflammatory ATM subpopulations including the newly identified metabolically active CD9 ATMs.

Macrophage-derived proinflammatory cytokines such as TNFα and IL1b have been reported to directly suppress the induction of UCP1 expression in adipocytes and to impair cold-induced thermogenesis in rodents (Goto *et al.*, 2016; Sakamoto *et al.*,

2016; Sakamoto *et al.*, 2013). Moreover, TNFα was shown to down-regulate the expression of β-adrenoceptor in adipocytes (Hadri et al., 1997; Valentine et al., 2022). HFD-induced obesity and chronic adipose inflammation are associated with the reduced expression of thermogenic/mitochondrial oxidation genes and the repression of thermogenesis (Choi et al., 2015). In present study, we observed that STF treatment increases the expression of UCP1, β_3-adrenoceptor, and other thermogenic genes in obese adipose tissue (Figs. 4L, N, O and S3D-F). These results suggest that the suppression of ATM population/inflammation by STF inhibition of IRE1α is able to reverse the expression levels of thermogenic/mitochondrial oxidation genes in obese adipose tissue to promote thermogenesis, in conjunction with STF's action on the PGC1α expression in adipocytes.

We noticed that STF treatment protects against diet-induced obesity (Fig. 2A-B) and metabolic improvements (Figs. 1-3). It exists a possibility that STF may cause body weight reduction, which results in secondary beneficial effects on glucose and insulin sensitivity, as well as on ATM accumulation. We argue that such a possibility is unlikely as STF was previously reported to have no effect on body weight in two other studies: one in mouse model of atherosclerosis (Tufanli *et al.*, 2017), and the other in Akita mouse model of beta cell death/failure (Herlea-Pana *et al.*, 2021). Second, in our study, we did not observe any apparent difference in food intake (Fig. S2B) that could otherwise affect body weight. Third, STF directly suppresses ATM population and pro-inflammatory gene expression. Finally, STF-treated DIO mice expended more energy than their vehicle-treated counterparts per mouse even at lower body weight (Fig. 4A-F). Although it is known that energy expenditure per unit body weight appears to be lower

in obese subjects than in lean controls because obesity is associated with reduced thermogenesis, obese subjects still expend more energy than the lean controls at the organismal level (Prentice et al., 1996; Trayhurn and Arch, 2020). If there exists leanness-associated thermogenesis increase per unit weight in STF-treated DIO mice, it cannot fully account for the energy expenditure increase at the organismal level as observed in STF-treated DIO mice, arguing for the notion that STF treatment stimulates thermogenesis which in turn leads to body weight reduce in a positive feedback loop.

Our study also shed new insight into the macrophage remodeling under obesity. Macrophage accumulation and activation in adipose tissue is known to contribute to insulin resistance in obesity. It was initially reported that adipose tissue macrophages (ATMs) undergo an M2 to M1 polarization switch under obesity. Recent studies have however indicated that obese ATMs do not follow the canonical M1 polarization (Hill *et al.*, 2018; Jaitin *et al.*, 2019; Kratz *et al.*, 2014; Xu *et al.*, 2013). In the present study, we found that first, “M1-like” ATMs (F4/80^{+}CD11b^{+}CD11c^{+}CD206^{-} cells) significantly increase under HFD (Fig. 5F-G, Table 1b-c); second, M2-like ATMs (F4/80^{+}CD11b^{+} CD206^{+}CD11c^{-} cells) also increase in total cell number and density in response to HFD (Table 1d), albeit to a smaller extent than the “M1-like” ATMs, a phenomenon previously reported (Xu *et al.*, 2013); and third, there is a significant increase (up to half of the ATMs gated with CD11c^{+} and CD206^{+}) in ATMs co-expressing both CD11c^{+} and CD206^{+} in the adipose tissue of HFD-induced obese mice (Fig. 5G, Table 1c), supporting a mixed phenotype rather than distinct M1 or M2 phenotype. Previous studies have identified such ATM subpopulation that express both M1 and M2 surface markers in both human and rodent adipose tissues under obesity (Shaul *et al.*, 2010;

Wentworth *et al.*, 2010). These findings are consistent with the notion that ATMs do not follow the classic M2 to M1 switch. Instead, recent studies employing single-cell RNA-seq technology have revealed the expansion/emergence of ATMs that express cell surface markers CD9 or Trem2 (Hill *et al.*, 2018; Jaitin *et al.*, 2019). In the present study, we found that the percentage, density, and total number of $CD9^+$ ATMs ($F4/80^+CD11b^+CD9^+$) in the eWAT are drastically increased under HFD (Fig. 6H, Table 2a). Similarly, $Trem2^+$ ATMs ($F4/80^+CD11b^+Trem2^+$) expand significantly in the eWAT of obese mice (Fig. 6I, Table 2b), most of which also express CD9.

Our present study further investigated the relationship between the newly-identified $CD9^+$ ATMs and the originally identified "M1-like" $CD11c^+$ ATMs as it remains unclear whether they are related or different ATM populations (Hill *et al.*, 2018; Wu and Ballantyne, 2020). Our results showed that CD9 and Trem2 are highly enriched but not exclusively expressed in the $CD11c^+$ ATMs under HFD (Fig. 7A-C). Reciprocally, CD11c expression is highly enriched but not exclusively expressed in $CD9^+$, $Trem2^+$, or $CD9^+Trem2^+$ ATMs (Fig. 7D-F). As such, in the obese eWAT, up to half ($49.95 \pm 0.65\%$) of ATMs co-express CD9 and CD11c (Fig. 7G). These results demonstrate that $CD9^+$ and $CD11c^+$ populations are highly overlapping. We further found that $CD9^+CD11c^-$, $CD9^-CD11c^+$, and $CD9^+CD11c^+$ ATMs are all pro-inflammatory as the mRNA levels of pro-inflammatory genes *TNFα*, *IL1b*, and *Mcp-1* are up-regulated in all these subpopulations than $CD9^-CD11c^-$ ATMs (Fig. 7H). However, the mRNA levels of individual *TNFα*, *IL1b*, or *Mcp-1* are differentially expressed among $CD9^+CD11c^-$, $CD9^-CD11c^+$, and $CD9^+CD11c^+$ ATMs (Fig. 7H), suggesting functional heterogeneity even among proinflammatory ATMs during obesity.

In summary, our present studies reveal two significant findings. First, we confirmed that the newly identified populations of proinflammatory ATMs (i.e., $CD9^+$ and $Trem2^+$) are induced under high fat diet-mediated obesity and determined their relationships with the originally identified "M1-like" $CD11c^+$ ATMs. Second, we showed that STF inhibition of IRE1α reverses the accumulation of pro-inflammatory ATM populations including the new metabolically active $CD9^+$ and $Trem2^+$ ATMs and adipose tissue inflammation to promote thermogenesis and insulin sensitivity. These studies validate the potential of IRE1α inhibitors for the prevention and treatment of obesity, insulin resistance and comorbidities, which sets the foundation for further clinical development of IRE1α inhibitors as a therapeutical direction for diabetes and obesity.

Funding

This work was supported by grants from the NIH (R01DK116017, R01DK128848, and R01DK130174) to W.W.

Author Contribution

Dan Wu, Venkateswararao Eeda, Zahra Maria, Komal Rawal, Oana Herlea-Pana, Ram Babu Undi: Methodology, Investigation, Formal analysis, Visualization, Validation, Original draft preparation. **Lim H-Y:** Conceptualization, Supervision, Writing - Reviewing and Editing. **Wang W:** Conceptualization, Supervision, Writing - Reviewing and Editing, Funding acquisition.

Acknowledgments

We thank the Diabetes CoBRE histology and Imaging (5P30GM122744) and Molecular Biology and Cytometry Research (P30CA225520) Cores at OUHSC for assistance on histology and microscopy use.

Conflict of Interest

None declared.

Figure legends:

Figure 1. IRE1α inhibitor STF improves glucose tolerance and insulin sensitivity in DIO mice. A. mRNA levels of ER stress genes in the eWAT from mice fed ND (normal diet) and HFD for 14 weeks, assessed by qRT-PCR. The results are expressed as fold change and are representative of 3 independent experiments. B. mRNA levels of IRE1α RIDD target genes in the eWAT from mice fed ND and HFD for 14 weeks, assessed by qRT-PCR. The results are expressed as fold change and are representative of 3 independent experiments. C-C'. Glucose tolerance test on mice treated with vehicle (n=7) or STF (n=8) at two weeks of treatment. Blood glucose levels (C) measured at indicated time points after intraperitoneal injection of glucose (1.5 g/kg body weight) following 6-h fasting and AOC (area of the curve, C'). D–D′. Insulin tolerance test on mice treated with vehicle (n = 7) or STF (n=8) at three weeks of treatment. Blood glucose levels (C) normalized to basal level at indicated time points after intraperitoneal injection of insulin (1.2 IU/kg body weight) following 6-h fasting and the AOC (area of the curve, D′). E. Plasma insulin levels at indicated time points after intraperitoneal injection of glucose (3 g/kg body weight) following 6-h fasting at 3.5 weeks of treatment. F-F'. Protein levels of pAKT and total AKT in eWAT of ND mice or DIO mice treated with vehicle or STF, analyzed with Western blotting (F). GAPDH as a loading control. Fasted mice were IP injected with either saline or insulin and scarified after 15 min and eWATs were collected. The data shown are representative of 3 independent experiments. Quantitative analysis of immunoblots was performed (F'). G-G'. Splicing of XBP1 mRNA was analyzed from eWAT of DIO mice treated with vehicle or STF by RT-PCR and resolved by agarose gel electrophoresis. The full length (unspliced, XBP1-u) and spliced (XBP1-s) forms of XBP1 mRNA were indicated (G) and quantified with t-XBP1 as the sum of XBP1-u and XBP1-s (G'). GAPDH mRNA was used as an internal control. The data shown are representative of 3 independent experiments. H. mRNA levels for indicated genes were analyzed in eWAT of DIO mice treated with vehicle or STF by qRT-PCR. The results were expressed as fold change and were representative of 3 independent experiments. Data were expressed as

mean ± SEM and analyzed using the unpaired two-tailed Student's t-test between two samples or ANOVA with multiple comparisons. $*P < 0.05$, $**P < 0.01$, and $***P < 0.001$.

Figure 2. STF protects against diet-induced adiposity and obesity. A. Body weight gain of DIO mice treated with vehicle (n=5) or STF (n=8) for 4 weeks. B. Fat mass and lean mass of DIO mice treated with vehicle or STF, assessed at the end of 4-week treatment by EchoMRI. C-E. eWAT adipocytes. Representative images of H&E staining of eWAT sections (C). Average diameter of adipocytes (μM)/field (D) and size distribution (E). F-H. iWAT adipocytes. Representative images of H&E staining of iWAT sections (F). Average diameter of adipocytes (μM)/field (G) and size distribution (H). I. Representative images of H&E staining of BAT. Data were expressed as mean ± SEM and analyzed using the unpaired two-tailed Student's t-test between two samples or ANOVA with multiple comparisons. $*P < 0.05$, $**P < 0.01$, and $***P < 0.001$.

Figure 3. STF treatment improves liver steatosis and dyslipidemia in DIO mice. A. Representative images of H&E of liver sections from mice of ND and HFD treated with vehicle or STF. B. mRNA levels of lipogenic genes in livers from DIO mice treated with vehicle or STF, assessed by qRT-PCR. The results are expressed as fold change and are representative of 3 independent experiments. C. mRNA levels of gluconeogenic genes in livers from DIO mice treated with vehicle or STF, assessed by qRT-PCR. The results are expressed as fold change and are representative of 3 independent experiments. D-E. Immunofluorescent staining of F4/80 in liver. Representative images of staining (D) and percentage of number of F4/80 positive cells over total cells/field (E). F-H. The levels of serum TG (F), FFA (G) and total cholesterol (H) were analyzed by respective ELISA kits. Blood samples were collected upon euthanization at the end of treatment. Data were expressed as mean ± SEM and analyzed using the unpaired two-tailed Student's t-test between two samples or ANOVA with multiple comparisons. $*P < 0.05$, $**P < 0.01$, and $***P < 0.001$.

Figure 4. STF promotes energy expenditure and thermogenesis in DIO mice. A-B. Curves (A) and quantification (B) of oxygen consumption levels. C-D. Curves (C) and quantification (D) of CO2 production levels. E-F. Curves (E) and quantification (F) of energy expenditure levels calculated. For A-F, the data was analyzed for group effect (ANOVA) along with the mass and interaction effects as necessary (generalized linear model, GLM). G. RER (respiratory exchange ratio) level. H. Daily activity (m of running distance/mouse). I-K. UCP1 immunofluorescence staining of BAT sections from ND-fed mice and DIO mice treated with vehicle or STF. Representative images of UCP1 immunofluorescence staining of BAT (I), quantification of immune-signal intensity of UCP1 (J), and quantification of UCP1-positive area (K). L. mRNA levels of thermogenic genes in BAT from DIO mice treated with vehicle or STF, assessed by qRT-PCR. The results are expressed as fold change and are representative of 3 independent experiments. M. Representative images of UCP1 immunofluorescence staining of eWAT sections from ND-fed mice and DIO mice treated with vehicle or STF. N. mRNA levels of thermogenic genes in eWAT from DIO mice treated with vehicle or STF, assessed by qRT-PCR. The results are expressed as fold change and are representative of 3 independent experiments. O. mRNA levels of β-adrenoceptor genes in BAT from DIO mice treated with vehicle or STF, assessed by qRT-PCR. The results were expressed as fold change and are representative of 3 independent experiments. Data for G-O were expressed as mean ± SEM and analyzed using the unpaired two-tailed Student's t-test between two samples or ANOVA with multiple comparisons. $*P < 0.05$, $**P < 0.01$, and $***P < 0.001$.

Figure 5. STF treatment suppresses ATM accumulation and adipose inflammation in DIO mice. A. Percentage of CLS area in eWAT sections from DIO mice treated with vehicle or STF. B-C. Immunofluorescent staining of F4/80 in the eWAT sections of DIO mice treated with vehicle or STF. Representative images of F4/80 in eWAT (B) and percentage of the number of F4/80-positive cells over total cells/field (C). D. mRNA levels of total macrophage marker genes in the SVF of eWAT from DIO mice treated with vehicle or STF, assessed by qRT-PCR. The results are expressed as fold change and are representative of 3 independent experiments. E. Flow cytometry of total ATMs

from eWAT SVFs of ND mice (n=4) and DIO mice treated with vehicle (n=4) or STF(n=4), gated against CD11b and F4/80 antibodies. Complete gating path was shown in Supplemental Figure 5A. F. Flow cytometry analysis of CD11C-positive ATMs ($F4/80^+CD11b^+CD11C^+$) from eWAT SVFs of mice with an overlay of gated CD11C marker for ND (yellow), HFD-Veh (blue) and HFD-STF (pink) shown. Complete gating path was shown in Supplemental Figure 5A. G. Flow cytometry of "M1-like" and "M2-like" subsets of ATMs from eWAT SVFs of ND, HFD-Veh and HFD-STF mice, gated against CD11c and CD206 antibodies. Complete gating path was shown in Supplemental Figure 5A. H. mRNA levels of indicated proinflammatory cytokine/chemokine genes in the SVF of eWAT of DIO mice treated with vehicle or STF, assessed by qRT-PCR. The results are expressed as fold change and are representative of 3 independent experiments. I. mRNA levels of indicated proinflammatory cytokine/chemokine genes in the indicated sorted cells from SVFs of eWAT of DIO mice, assessed by qRT-PCR. The results are expressed as fold change and are representative of 3 independent experiments. J. mRNA levels of indicated proinflammatory cytokine/chemokine genes in the $CD11C^+$ ATMs ($F4/80^+CD11b^+CD11C^+$) sorted from SVFs of eWAT of DIO mice treated with vehicle or STF, assessed by qRT-PCR. The results were expressed as fold change and were representative of 3 independent experiments. Data were expressed as mean ± SEM and analyzed using the unpaired two-tailed Student's t-test between two samples or ANOVA with multiple comparisons. $*P < 0.05$, $**P < 0.01$, and $***P < 0.001$.

Figure 6. STF suppresses the accumulation of metabolically active CD9 or Trem2-expressing ATMs in obesity. A-D. mRNA levels of indicated genes in the SVFs of eWAT from ND, HFD-veh and HFD-STF mice, assessed by qRT-PCR. The results are expressed as fold change and are representative of 3 independent experiments. E-G. Immunofluorescent staining of CD9 and Trem2 in the eWAT sections of DIO mice treated with vehicle or STF. Representative images shown (E) and percentages of the numbers of CD9-positive cells (F) and Trem2-positive cells (G) over total cells/field. H. Analysis of CD9-positive ATMs ($F4/80^+CD11b^+CD9^+$) from eWAT SVFs of mice with an overlay of gated CD9 marker for ND (blue), HFD-Veh (yellow) and HFD-STF (pink)

shown. Complete gating path was shown in Supplemental Figure 5. I. Analysis of Trem2-positive ATMs ($F4/80^+CD11b^+Trem2^+$) from eWAT SVFs of mice with an overlay of gated Trem2 marker for ND (blue), HFD-Veh (yellow) and HFD-STF (pink) shown. Complete gating path was shown in Supplemental Figure 5A. J. Flow cytometry analysis of $CD9^+$ and $Trem2^+$ ATMs from eWAT SVFs of ND, HFD-Veh and HFD-STF mice, gated against CD9 and Trem2 antibodies. Complete gating path was shown in Supplemental Figure 5A. K-L. mRNA levels of indicated proinflammatory genes in the indicated cells sorted from SVFs of eWAT of DIO mice, assessed by qRT-PCR: for $CD9^+$ vs $CD9^-$ ATMs (K) and for $Trem2^+$ vs $Trem2^-$ ATMs (L). The results are expressed as fold change and are representative of 3 independent experiments. M-N. mRNA levels of indicated proinflammatory cytokine/chemokine genes in the $CD9^+$ ATMs ($F4/80^+CD11b^+CD9^+$) (M) and the $Trem2^+$ ATMs ($F4/80^+CD11b^+Trem2^+$) (N) sorted from SVFs of eWAT of DIO mice treated with vehicle or STF, assessed by qRT-PCR. The results were expressed as fold change and are representative of 3 independent experiments. O-P. Flow cytometry analysis of ATMs from SVFs of the eWAT from 20-week HFD-fed mice. SVFs were cultured and treated with 0.01% DMSO control or STF (30 μM) for 20 h followed by staining and flow analysis, gated against F4/80 and CD11b antibodies (O) and further gated against Trem2 antibody (P). The gating path followed the one as Supplemental Figure 5A. Q-S. mRNA levels of indicated genes in $CD9^+$ ATMs (Q and R) and in $CD11C^+$ ATMs (S) sorted from SVFs cultured and treated with DMSO or STF as in O-P, assessed by qRT-PCR. Data were expressed as mean ± SEM and analyzed using the unpaired two-tailed Student's t-test between two samples or ANOVA with multiple comparisons. $*P < 0.05$, $**P < 0.01$, and $***P < 0.001$.

Figure 7. The relationship of $CD11c^+$ ATMs with metabolically active $CD9^+$ or $Trem2^+$ ATMs in DIO mice. A. Overlay of the flow cytometric analysis of percentages of CD9-positive signals among $CD11C\text{-}^{hi}$ (pink), $CD11C^+$ (yellow), and $CD11C^-$ (blue) ATMs from eWAT SVFs of DIO mice. B-C. Overlay of the flow cytometric analysis of percentages of CD9-positive (B) and CD9-and Trem2-doubly positive (C) signals among $CD11C^+$ (yellow) and $CD11C^-$ (blue/green) ATMs from eWAT SVFs of DIO mice. D-F. Overlay of the flow cytometric analysis of percentages of CD11-positive signals among

CD9$^{hi, +, and -}$ ATMs (D), Trem2$^{+ and -}$ ATMs (E), and CD9/Trem2$^{+ and -}$ ATMs (F) from eWAT SVFs of DIO mice. The gating strategies for A-F were shown in Supplemental Figure 9. G. Flow cytometry of CD9^{+} and CD11C^{+} ATMs from eWAT SVFs of DIO mice treated with vehicle or STF, gated against CD9 and CD11C antibodies. Complete gating path was shown in Supplemental Figure 5A. H. mRNA levels of indicated proinflammatory cytokine/chemokine genes in the indicated ATM subpopulations sorted from SVFs of eWAT of DIO, assessed by qRT-PCR. The results were expressed as fold change and were representative of 3 independent experiments. Data were expressed as mean ± SEM and analyzed using the unpaired two-tailed Student's t-test between two samples or ANOVA with multiple comparisons. $*P < 0.05$, $**P < 0.01$, and $***P < 0.001$.

Table 1. Effect of STF treatment on "M1-like" and "M2-like" ATMs in obesity. a. The total number and density of ATMs (F4/80^{+}CD11B^{+}) in eWAT in mice with ND, HFD-Veh, or HFD-STF. b. The percentage, total cell number, and density of CD11C^{+} ATMs in eWAT in mice with ND, HFD-Veh, or HFD-STF. c. The total cell number and density of C11DC^{+} CD206^{+}ATMs in eWAT in mice with ND, HFD-Veh, or HFD-STF. d. The total cell number and density of CD206^{+}C11DC^{-} ATMs in eWAT in mice with ND, HFD-Veh, or HFD-STF. Data in a-d were obtained from 2 batches of 4-5 mice each and were expressed as mean ± SEM and analyzed using the unpaired two-tailed Student's t-test between two samples or ANOVA with multiple comparisons. $*P < 0.05$, $**P < 0.01$, and $***P < 0.001$.

Table 2. Characterization of and the effect of STF treatment on CD9^{+} and Trem2^{+} ATMs in DIO mice. The percentage, total cell number, and density of subpopulations of CD9^{+} ATMs (a), Trem2^{+} ATMs (b), and CD9^{+} Trem2^{+} ATMs(c) in eWAT from mice with ND, HFD-Veh, or HFD-STF. Data in a-c were obtained from 2 batches of 4-5 mice each and were expressed as mean ± SEM and analyzed using the unpaired two-tailed Student's t-test between two samples or ANOVA with multiple comparisons. $*P < 0.05$, $**P < 0.01$, and $***P < 0.001$.

Table 3. **Flow cytometry analysis of relationship between "M1-like" ATMs and $CD9^+$ /$Trem2^+$ ATMs.** a. The percentages of cells expressing CD9, Trem2 or both CD9 and Trem2 markers in $CD11c^+$ or $CD11c^-$ ATMs from eWATs of DIO mice. b. The percentages of cells expressing CD11C marker in $CD9^+$, $Trem2^+$, or $CD9^+$ $Trem2^+$ ATMs versus their negative counterparts from eWATs of DIO mice. c. The percentage, total cell number, and density of $CD9^+$ $CD11c^+$ ATMs from eWATs of DIO mice treated with vehicle or STF. Data in a-c were obtained from 2 batches of 4-5 mice each and were expressed as mean ± SEM and analyzed using the unpaired two-tailed Student's t-test between two samples or ANOVA with multiple comparisons. $*P < 0.05$, $**P < 0.01$, and $***P < 0.001$.

References:

Asada, R., Kanemoto, S., Matsuhisa, K., Hino, K., Cui, M., Cui, X., Kaneko, M., and Imaizumi, K. (2015). IRE1α-XBP1 is a novel branch in the transcriptional regulation of Ucp1 in brown adipocytes. Scientific reports *5*, 16580. 10.1038/srep16580.

Back, S.H., and Kaufman, R.J. (2012). Endoplasmic reticulum stress and type 2 diabetes. Annual review of biochemistry *81*, 767-793. 10.1146/annurev-biochem-072909-095555.

Boden, G., Duan, X., Homko, C., Molina, E.J., Song, W., Perez, O., Cheung, P., and Merali, S. (2008a). Increase in endoplasmic reticulum stress-related proteins and genes in adipose tissue of obese, insulin-resistant individuals. Diabetes *57*, 2438-2444. 10.2337/db08-0604.

Boden, G., Duan, X., Homko, C., Molina, E.J., Song, W., Perez, O., Cheung, P., and Merali, S. (2008b). Increase in Endoplasmic Reticulum Stress–Related Proteins and Genes in Adipose Tissue of Obese, Insulin-Resistant Individuals. Diabetes *57*, 2438-2444. 10.2337/db08-0604.

Chen, Y., Wu, Z., Huang, S., Wang, X., He, S., Liu, L., Hu, Y., Chen, L., Chen, P., Liu, S., et al. (2022). Adipocyte IRE1α promotes PGC1α mRNA decay and restrains adaptive thermogenesis. Nat Metab *4*, 1166-1184. 10.1038/s42255-022-00631-8.

Choi, M.S., Kim, Y.J., Kwon, E.Y., Ryoo, J.Y., Kim, S.R., and Jung, U.J. (2015). High-fat diet decreases energy expenditure and expression of genes controlling lipid metabolism, mitochondrial function and skeletal system development in the adipose tissue, along with increased expression of extracellular matrix remodelling- and inflammation-related genes. Br J Nutr *113*, 867-877. 10.1017/s0007114515000100.

Cinti, S., Mitchell, G., Barbatelli, G., Murano, I., Ceresi, E., Faloia, E., Wang, S., Fortier, M., Greenberg, A.S., and Obin, M.S. (2005). Adipocyte death defines macrophage localization and function in adipose tissue of obese mice and humans. Journal of lipid research *46*, 2347-2355. 10.1194/jlr.M500294-JLR200.

Cnop, M., Foufelle, F., and Velloso, L.A. (2012). Endoplasmic reticulum stress, obesity and diabetes. Trends in Molecular Medicine *18*, 59-68. https://doi.org/10.1016/j.molmed.2011.07.010.

Coats, B.R., Schoenfelt, K.Q., Barbosa-Lorenzi, V.C., Peris, E., Cui, C., Hoffman, A., Zhou, G., Fernandez, S., Zhai, L., Hall, B.A., et al. (2017). Metabolically Activated Adipose Tissue Macrophages Perform Detrimental and Beneficial Functions during Diet-Induced Obesity. Cell reports *20*, 3149-3161. 10.1016/j.celrep.2017.08.096.

Fischer, K., Ruiz, H.H., Jhun, K., Finan, B., Oberlin, D.J., van der Heide, V., Kalinovich, A.V., Petrovic, N., Wolf, Y., Clemmensen, C., et al. (2017). Alternatively activated macrophages do not synthesize catecholamines or contribute to adipose tissue adaptive thermogenesis. Nat Med *23*, 623-630. 10.1038/nm.4316.

Foley, K.P., Chen, Y., Barra, N.G., Heal, M., Kwok, K., Tamrakar, A.K., Chi, W., Duggan, B.M., Henriksbo, B.D., Liu, Y., and Schertzer, J.D. (2021). Inflammation promotes adipocyte lipolysis via IRE1 kinase. The Journal of biological chemistry *296*, 100440. 10.1016/j.jbc.2021.100440.

Fonseca, S.G., Gromada, J., and Urano, F. (2011). Endoplasmic reticulum stress and pancreatic beta-cell death. Trends in endocrinology and metabolism: TEM *22*, 266-274. 10.1016/j.tem.2011.02.008.

Goto, T., Naknukool, S., Yoshitake, R., Hanafusa, Y., Tokiwa, S., Li, Y., Sakamoto, T., Nitta, T., Kim, M., Takahashi, N., et al. (2016). Proinflammatory cytokine interleukin-1β suppresses cold-induced thermogenesis in adipocytes. Cytokine *77*, 107-114. 10.1016/j.cyto.2015.11.001.

Gregor, M.F., Yang, L., Fabbrini, E., Mohammed, B.S., Eagon, J.C., Hotamisligil, G.S., and Klein, S. (2009). Endoplasmic reticulum stress is reduced in tissues of obese subjects after weight loss. Diabetes *58*, 693-700. 10.2337/db08-1220.

Hadri, K.E., Courtalon, A., Gauthereau, X., Chambaut-Guérin, A.-M., Pairault, J., and Fève, B. (1997). Differential Regulation by Tumor Necrosis Factor-α of β1-, β2-, and β3-Adrenoreceptor Gene Expression

in 3T3-F442A Adipocytes*. Journal of Biological Chemistry *272*, 24514-24521. https://doi.org/10.1074/jbc.272.39.24514.

Herlea-Pana, O., Eeda, V., Undi, R.B., Lim, H.-Y., and Wang, W. (2021). Pharmacological Inhibition of Inositol-Requiring Enzyme 1α RNase Activity Protects Pancreatic Beta Cell and Improves Diabetic Condition in Insulin Mutation-Induced Diabetes. Frontiers in Endocrinology *12*. 10.3389/fendo.2021.749879.

Hetz, C., Chevet, E., and Harding, H.P. (2013). Targeting the unfolded protein response in disease. Nature reviews. Drug discovery *12*, 703-719. 10.1038/nrd3976.

Hill, D.A., Lim, H.W., Kim, Y.H., Ho, W.Y., Foong, Y.H., Nelson, V.L., Nguyen, H.C.B., Chegireddy, K., Kim, J., Habertheuer, A., et al. (2018). Distinct macrophage populations direct inflammatory versus physiological changes in adipose tissue. Proceedings of the National Academy of Sciences of the United States of America *115*, E5096-e5105. 10.1073/pnas.1802611115.

Jaitin, D.A., Adlung, L., Thaiss, C.A., Weiner, A., Li, B., Descamps, H., Lundgren, P., Bleriot, C., Liu, Z., Deczkowska, A., et al. (2019). Lipid-Associated Macrophages Control Metabolic Homeostasis in a Trem2-Dependent Manner. Cell *178*, 686-698.e614. 10.1016/j.cell.2019.05.054.

Kajimura, S., Spiegelman, B.M., and Seale, P. (2015). Brown and Beige Fat: Physiological Roles beyond Heat Generation. Cell metabolism *22*, 546-559. 10.1016/j.cmet.2015.09.007.

Kapuy, O., Márton, M., Bánhegyi, G., and Vinod, P.K. (2020). Multiple system-level feedback loops control life-and-death decisions in endoplasmic reticulum stress. FEBS Lett *594*, 1112-1123. 10.1002/1873-3468.13689.

Kawasaki, N., Asada, R., Saito, A., Kanemoto, S., and Imaizumi, K. (2012). Obesity-induced endoplasmic reticulum stress causes chronic inflammation in adipose tissue. Scientific reports *2*, 799. 10.1038/srep00799.

Khan, R.S., Bril, F., Cusi, K., and Newsome, P.N. (2019). Modulation of Insulin Resistance in Nonalcoholic Fatty Liver Disease. Hepatology (Baltimore, Md.) *70*, 711-724. 10.1002/hep.30429.

Kratz, M., Coats, B.R., Hisert, K.B., Hagman, D., Mutskov, V., Peris, E., Schoenfelt, K.Q., Kuzma, J.N., Larson, I., Billing, P.S., et al. (2014). Metabolic dysfunction drives a mechanistically distinct proinflammatory phenotype in adipose tissue macrophages. Cell metabolism *20*, 614-625. 10.1016/j.cmet.2014.08.010.

Lefere, S., and Tacke, F. (2019). Macrophages in obesity and non-alcoholic fatty liver disease: Crosstalk with metabolism. JHEP Rep *1*, 30-43. 10.1016/j.jhepr.2019.02.004.

Lerner, Alana G., Upton, J.-P., Praveen, P.V.K., Ghosh, R., Nakagawa, Y., Igbaria, A., Shen, S., Nguyen, V., Backes, Bradley J., Heiman, M., et al. (2012). IRE1α Induces Thioredoxin-Interacting Protein to Activate the NLRP3 Inflammasome and Promote Programmed Cell Death under Irremediable ER Stress. Cell metabolism *16*, 250-264. https://doi.org/10.1016/j.cmet.2012.07.007.

Lumeng, C.N., Bodzin, J.L., and Saltiel, A.R. (2007). Obesity induces a phenotypic switch in adipose tissue macrophage polarization. The Journal of clinical investigation *117*, 175-184. 10.1172/jci29881.

Marchesini, G., Brizi, M., Bianchi, G., Tomassetti, S., Bugianesi, E., Lenzi, M., McCullough, A.J., Natale, S., Forlani, G., and Melchionda, N. (2001). Nonalcoholic fatty liver disease: a feature of the metabolic syndrome. Diabetes *50*, 1844-1850. 10.2337/diabetes.50.8.1844.

Marciniak, S.J., Chambers, J.E., and Ron, D. (2021). Pharmacological targeting of endoplasmic reticulum stress in disease. Nature reviews. Drug discovery. 10.1038/s41573-021-00320-3.

Martinon, F., Chen, X., Lee, A.H., and Glimcher, L.H. (2010). TLR activation of the transcription factor XBP1 regulates innate immune responses in macrophages. Nature immunology *11*, 411-418. 10.1038/ni.1857.

Márton, M., Kurucz, A., Lizák, B., Margittai, É., Bánhegyi, G., and Kapuy, O. (2017). A Systems Biological View of Life-and-Death Decision with Respect to Endoplasmic Reticulum Stress—The Role of PERK Pathway. International Journal of Molecular Sciences *18*, 58.

Mina, A.I., LeClair, R.A., LeClair, K.B., Cohen, D.E., Lantier, L., and Banks, A.S. (2018). CalR: A Web-Based Analysis Tool for Indirect Calorimetry Experiments. Cell metabolism *28*, 656-666.e651. 10.1016/j.cmet.2018.06.019.

Nguyen, K.D., Qiu, Y., Cui, X., Goh, Y.P., Mwangi, J., David, T., Mukundan, L., Brombacher, F., Locksley, R.M., and Chawla, A. (2011). Alternatively activated macrophages produce catecholamines to sustain adaptive thermogenesis. Nature *480*, 104-108. 10.1038/nature10653.

Oslowski, C.M., Hara, T., O'Sullivan-Murphy, B., Kanekura, K., Lu, S., Hara, M., Ishigaki, S., Zhu, L.J., Hayashi, E., Hui, S.T., et al. (2012). Thioredoxin-interacting protein mediates ER stress-induced β cell death through initiation of the inflammasome. Cell metabolism *16*, 265-273. 10.1016/j.cmet.2012.07.005.

Ozcan, U., Cao, Q., Yilmaz, E., Lee, A.H., Iwakoshi, N.N., Ozdelen, E., Tuncman, G., Görgün, C., Glimcher, L.H., and Hotamisligil, G.S. (2004). Endoplasmic reticulum stress links obesity, insulin action, and type 2 diabetes. Science (New York, N.Y.) *306*, 457-461. 10.1126/science.1103160.

Papa, F.R. (2012). Endoplasmic reticulum stress, pancreatic beta-cell degeneration, and diabetes. Cold Spring Harbor perspectives in medicine *2*, a007666. 10.1101/cshperspect.a007666.

Papandreou, I., Denko, N.C., Olson, M., Van Melckebeke, H., Lust, S., Tam, A., Solow-Cordero, D.E., Bouley, D.M., Offner, F., Niwa, M., and Koong, A.C. (2011). Identification of an Ire1alpha endonuclease specific inhibitor with cytotoxic activity against human multiple myeloma. Blood *117*, 1311-1314. 10.1182/blood-2010-08-303099.

Prentice, A.M., Black, A.E., Coward, W.A., and Cole, T.J. (1996). Energy expenditure in overweight and obese adults in affluent societies: an analysis of 319 doubly-labelled water measurements. Eur J Clin Nutr *50*, 93-97.

Sakamoto, T., Nitta, T., Maruno, K., Yeh, Y.S., Kuwata, H., Tomita, K., Goto, T., Takahashi, N., and Kawada, T. (2016). Macrophage infiltration into obese adipose tissues suppresses the induction of UCP1 level in mice. American journal of physiology. Endocrinology and metabolism *310*, E676-e687. 10.1152/ajpendo.00028.2015.

Sakamoto, T., Takahashi, N., Sawaragi, Y., Naknukool, S., Yu, R., Goto, T., and Kawada, T. (2013). Inflammation induced by RAW macrophages suppresses UCP1 mRNA induction via ERK activation in 10T1/2 adipocytes. Am J Physiol Cell Physiol *304*, C729-738. 10.1152/ajpcell.00312.2012.

Sha, H., He, Y., Chen, H., Wang, C., Zenno, A., Shi, H., Yang, X., Zhang, X., and Qi, L. (2009). The IRE1alpha-XBP1 pathway of the unfolded protein response is required for adipogenesis. Cell metabolism *9*, 556-564. 10.1016/j.cmet.2009.04.009.

Shan, B., Wang, X., Wu, Y., Xu, C., Xia, Z., Dai, J., Shao, M., Zhao, F., He, S., Yang, L., et al. (2017). The metabolic ER stress sensor IRE1α suppresses alternative activation of macrophages and impairs energy expenditure in obesity. Nature immunology *18*, 519-529. 10.1038/ni.3709.

Shaul, M.E., Bennett, G., Strissel, K.J., Greenberg, A.S., and Obin, M.S. (2010). Dynamic, M2-like remodeling phenotypes of CD11c+ adipose tissue macrophages during high-fat diet--induced obesity in mice. Diabetes *59*, 1171-1181. 10.2337/db09-1402.

Sica, A., and Mantovani, A. (2012). Macrophage plasticity and polarization: in vivo veritas. The Journal of clinical investigation *122*, 787-795. 10.1172/jci59643.

Trayhurn, P., and Arch, J.R.S. (2020). Is energy expenditure reduced in obese mice with mutations in the leptin/leptin receptor genes? J Nutr Sci *9*, e23. 10.1017/jns.2020.19.

Tsuru, A., Fujimoto, N., Takahashi, S., Saito, M., Nakamura, D., Iwano, M., Iwawaki, T., Kadokura, H., Ron, D., and Kohno, K. (2013). Negative feedback by IRE1beta optimizes mucin production in goblet cells. Proceedings of the National Academy of Sciences of the United States of America *110*, 2864-2869. 10.1073/pnas.1212484110.

Tufanli, O., Telkoparan Akillilar, P., Acosta-Alvear, D., Kocaturk, B., Onat, U.I., Hamid, S.M., Çimen, I., Walter, P., Weber, C., and Erbay, E. (2017). Targeting IRE1 with small molecules counteracts progression

of atherosclerosis. Proceedings of the National Academy of Sciences *114*, E1395. 10.1073/pnas.1621188114.

Valentine, J.M., Ahmadian, M., Keinan, O., Abu-Odeh, M., Zhao, P., Zhou, X., Keller, M.P., Gao, H., Yu, R.T., Liddle, C., et al. (2022). β3-Adrenergic receptor downregulation leads to adipocyte catecholamine resistance in obesity. The Journal of clinical investigation *132*. 10.1172/jci153357.

Weisberg, S.P., McCann, D., Desai, M., Rosenbaum, M., Leibel, R.L., and Ferrante Jr, A.W. (2003). Obesity is associated with macrophage accumulation in adipose tissue. Journal of Clinical Investigation *112*, 1796-1808. 10.1172/JCI200319246.

Wentworth, J.M., Naselli, G., Brown, W.A., Doyle, L., Phipson, B., Smyth, G.K., Wabitsch, M., O'Brien, P.E., and Harrison, L.C. (2010). Pro-inflammatory CD11c+CD206+ adipose tissue macrophages are associated with insulin resistance in human obesity. Diabetes *59*, 1648-1656. 10.2337/db09-0287.

Wu, H., and Ballantyne, C.M. (2020). Metabolic Inflammation and Insulin Resistance in Obesity. Circulation research *126*, 1549-1564. 10.1161/circresaha.119.315896.

Xu, H., Barnes, G.T., Yang, Q., Tan, G., Yang, D., Chou, C.J., Sole, J., Nichols, A., Ross, J.S., Tartaglia, L.A., and Chen, H. (2003). Chronic inflammation in fat plays a crucial role in the development of obesity-related insulin resistance. Journal of Clinical Investigation *112*, 1821-1830. 10.1172/JCI200319451.

Xu, X., Grijalva, A., Skowronski, A., van Eijk, M., Serlie, M.J., and Ferrante, A.W., Jr. (2013). Obesity activates a program of lysosomal-dependent lipid metabolism in adipose tissue macrophages independently of classic activation. Cell metabolism *18*, 816-830. 10.1016/j.cmet.2013.11.001.

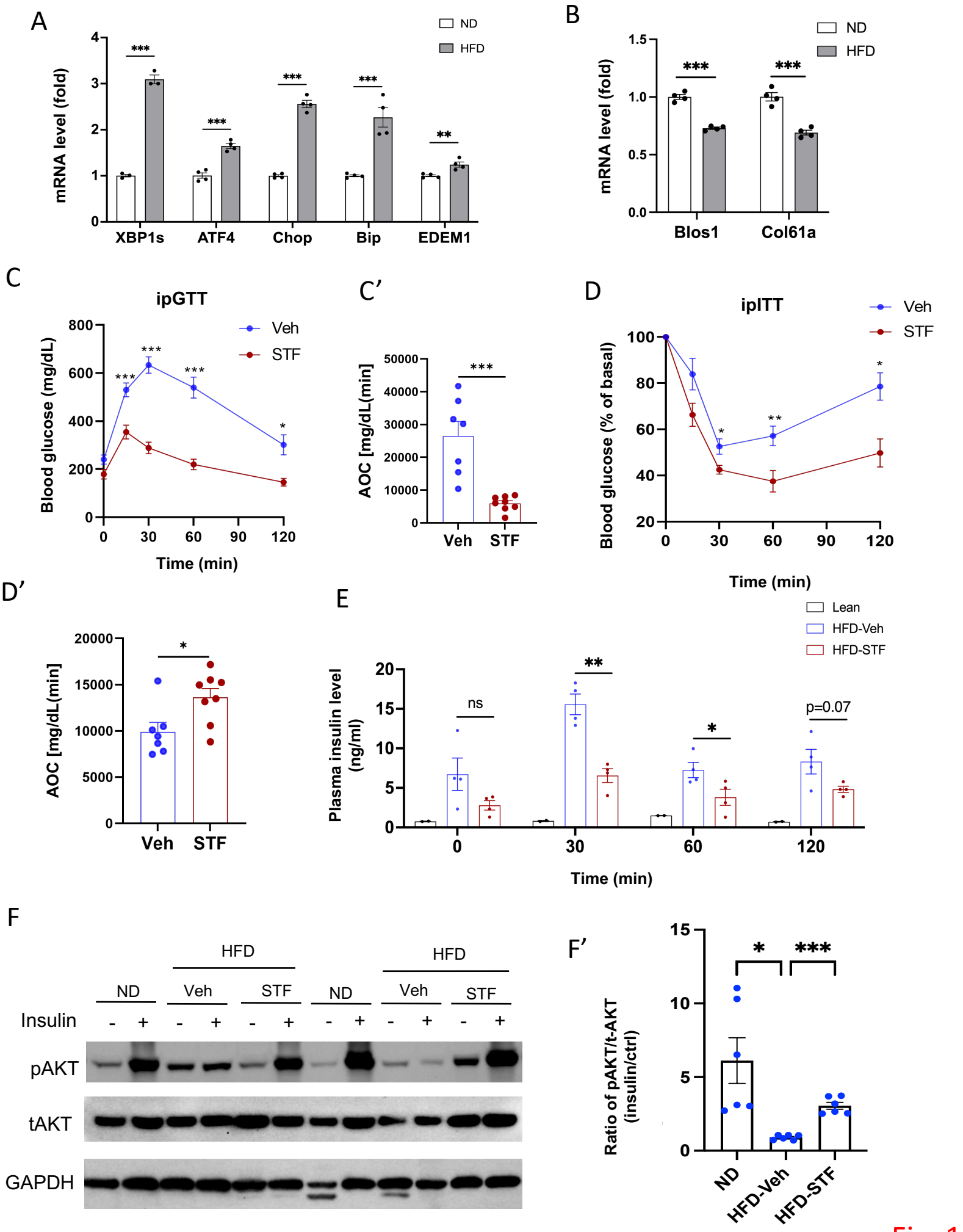
A
ND
HFD
mRNA level (fold)
XBP1s
ATF4
Chop
Bip
EDEM1
B
Blos1
Col61a
C
ipGTT
Veh
STF
Blood glucose (mg/dL)
Time (min)
C'
AOC [mg/dL(min]
D
ipITT
Blood glucose (% of basal)
D'
E
Lean
HFD-Veh
HFD-STF
Plasma insulin level (ng/ml)
ns
p=0.07
F
HFD
Insulin
pAKT
tAKT
GAPDH
F'
Ratio of pAKT/t-AKT (insulin/ctrl)

Fig. 1

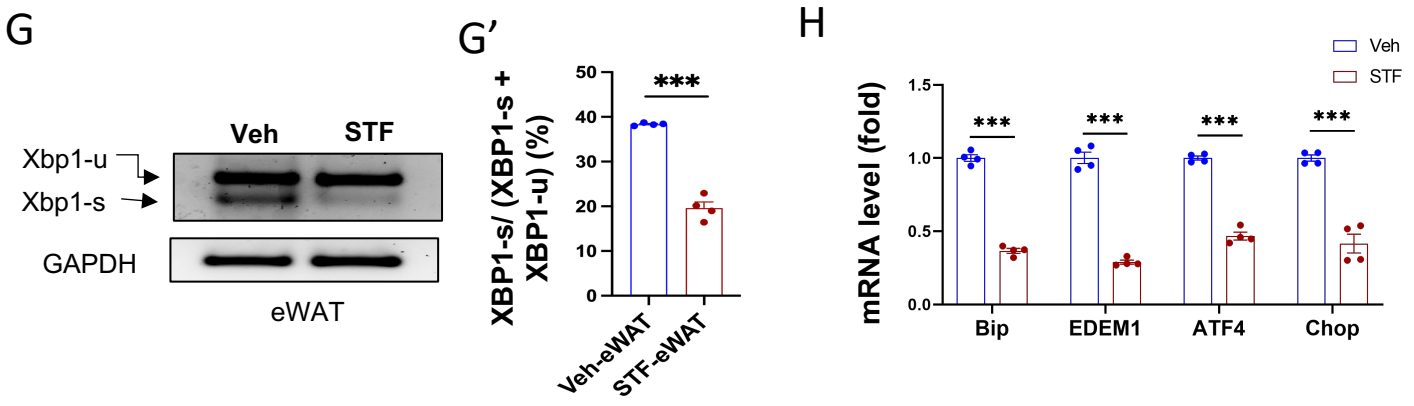
G
Veh
STF
Xbp1-u
Xbp1-s
GAPDH
eWAT
G'
XBP1-s/ (XBP1-s + XBP1-u) (%)
50
40
30
20
10
0
***
Veh-eWAT
STF-eWAT
H
Veh
STF
mRNA level (fold)
1.5
1.0
0.5
0.0
***
Bip
EDEM1
ATF4
Chop

Fig. 1 (conti.)

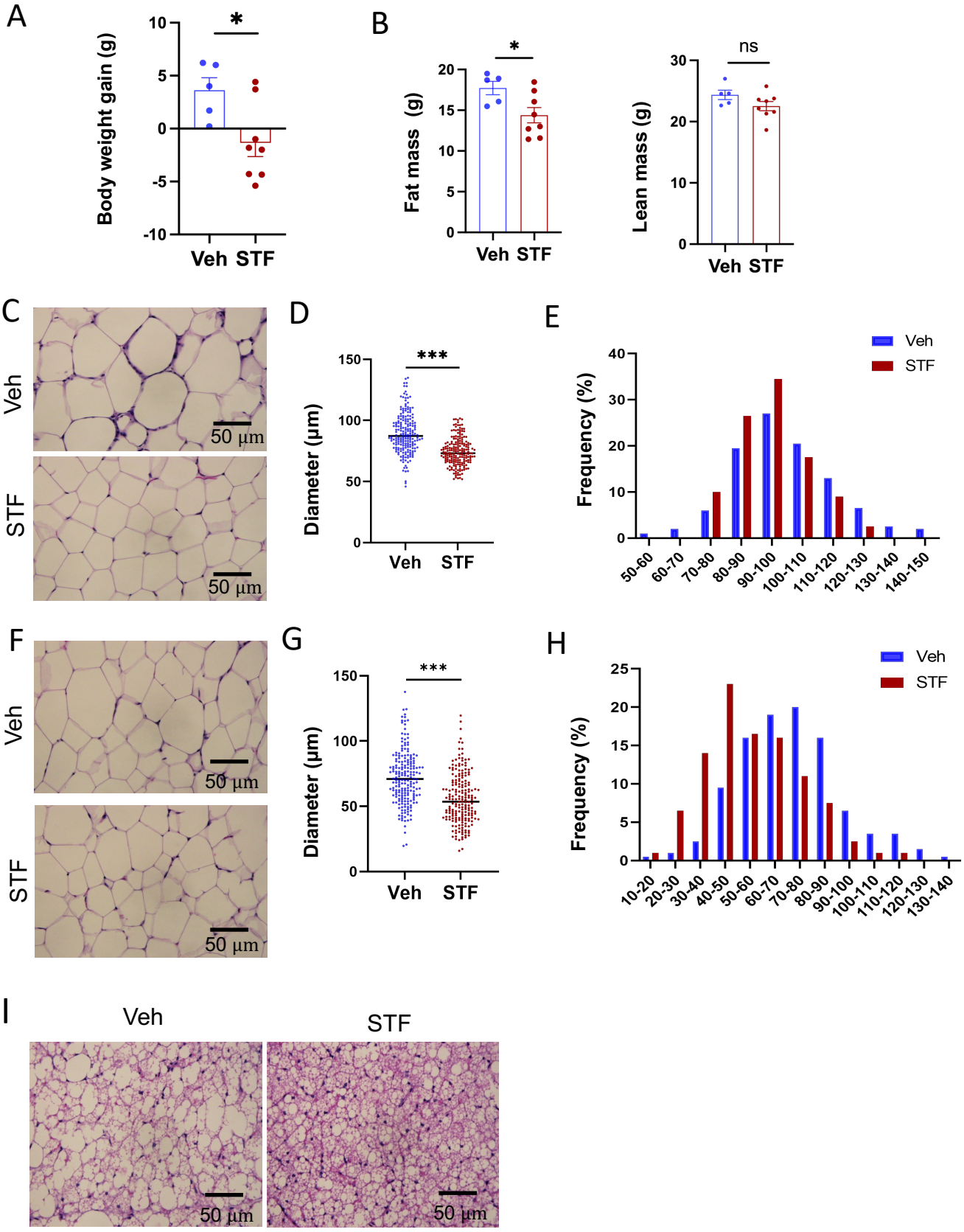
A
Body weight gain (g)
10
5
0
-5
-10
*
Veh STF
B
Fat mass (g)
20
15
10
5
0
*
Veh STF
Lean mass (g)
30
20
10
0
ns
Veh STF
C
Veh
STF
50 µm
50 µm
D
Diameter (µm)
150
100
50
0
***
Veh STF
E
Frequency (%)
40
30
20
10
0
Veh
STF
50-60
60-70
70-80
80-90
90-100
100-110
110-120
120-130
130-140
140-150
F
Veh
STF
50 µm
50 µm
G
Diameter (µm)
150
100
50
0
***
Veh STF
H
Frequency (%)
25
20
15
10
5
0
Veh
STF
10-20
20-30
30-40
40-50
50-60
60-70
70-80
80-90
90-100
100-110
110-120
120-130
130-140
I
Veh
STF
50 µm
50 µm

Fig. 2

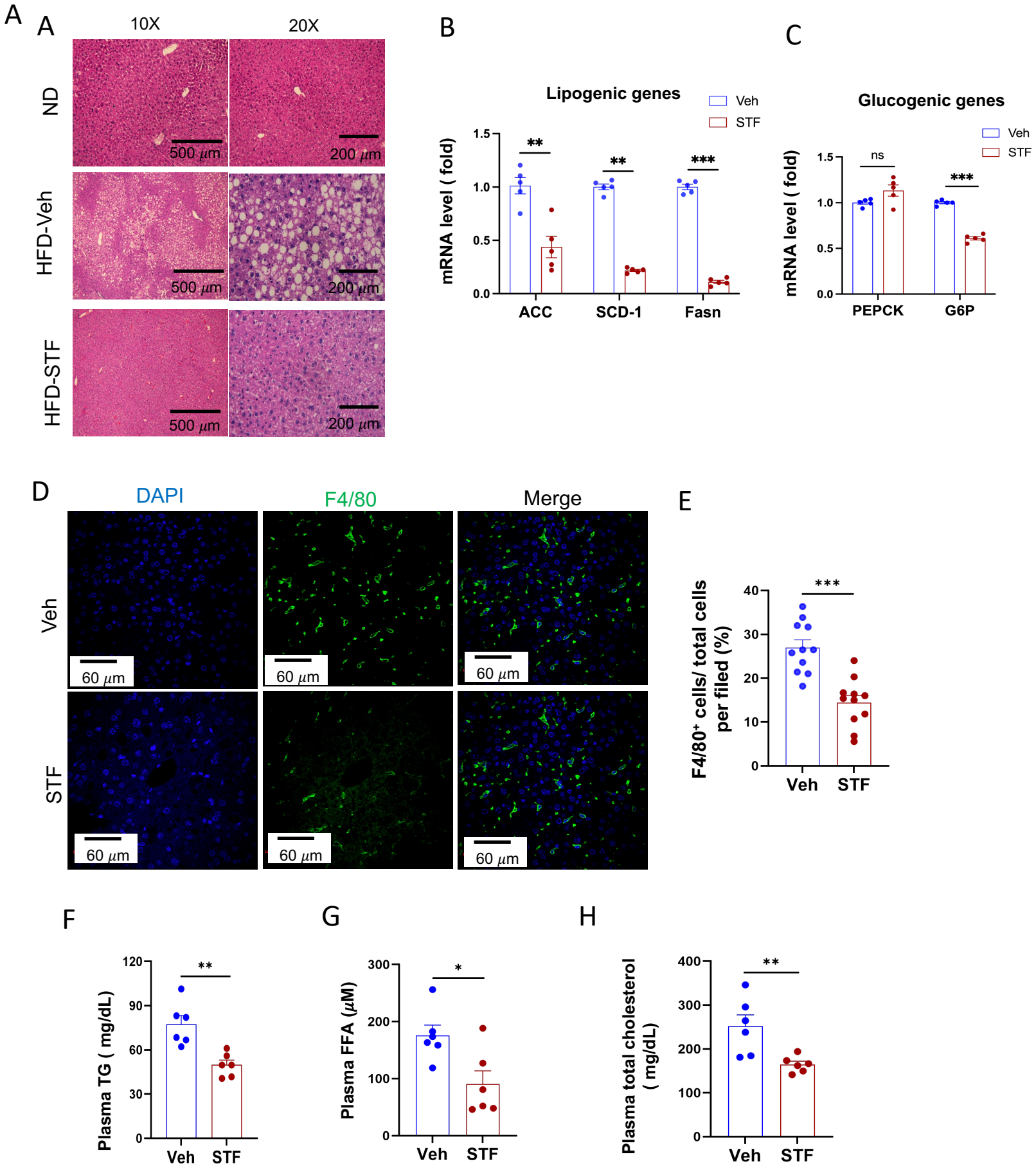
A
10X
20X
ND
HFD-Veh
HFD-STF
500 μm
200 μm
B
Lipogenic genes
Veh
STF
mRNA level (fold)
1.5
1.0
0.5
0.0
**
**
***
ACC
SCD-1
Fasn
C
Glucogenic genes
Veh
STF
mRNA level (fold)
ns
***
PEPCK
G6P
D
DAPI
F4/80
Merge
Veh
STF
60 μm
E
F4/80⁺ cells/ total cells per filed (%)
40
30
20
10
0
***
Veh
STF
F
Plasma TG (mg/dL)
120
90
60
30
0
**
Veh
STF
G
Plasma FFA (μM)
300
200
100
0
*
Veh
STF
H
Plasma total cholesterol (mg/dL)
400
300
200
100
0
**
Veh
STF

Fig. 3

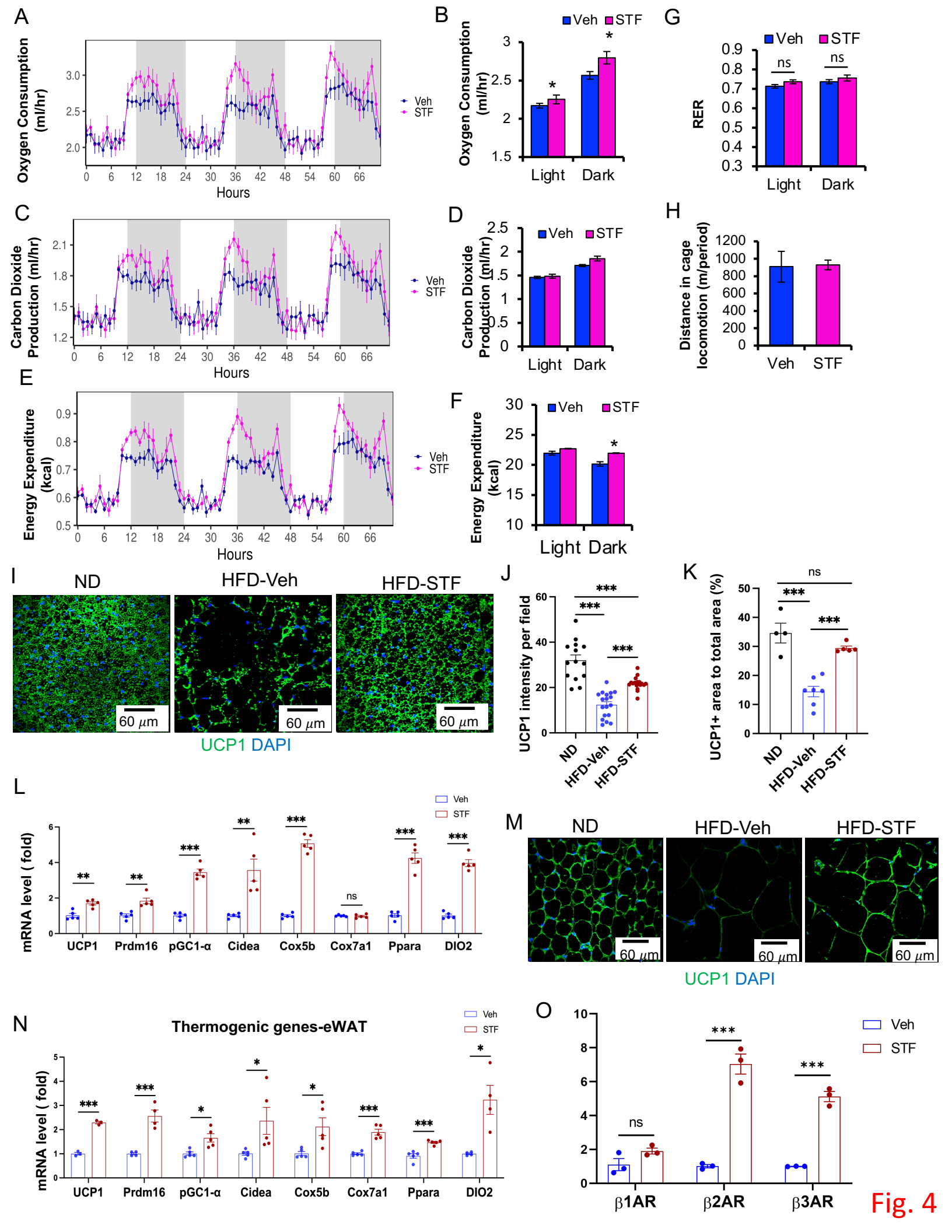
A
Oxygen Consumption (ml/hr)
Hours
Veh
STF
B
Oxygen Consumption (ml/hr)
Veh
STF
Light
Dark
G
RER
ns
C
Carbon Dioxide Production (ml/hr)
D
H
Distance in cage locomotion (m/period)
E
Energy Expenditure (kcal)
F
I
ND
HFD-Veh
HFD-STF
60 μm
UCP1 DAPI
J
UCP1 intensity per field
K
UCP1+ area to total area (%)
L
mRNA level (fold)
UCP1
Prdm16
pGC1-α
Cidea
Cox5b
Cox7a1
Ppara
DIO2
M
N
Thermogenic genes-eWAT
O
β1AR
β2AR
β3AR

Fig. 4

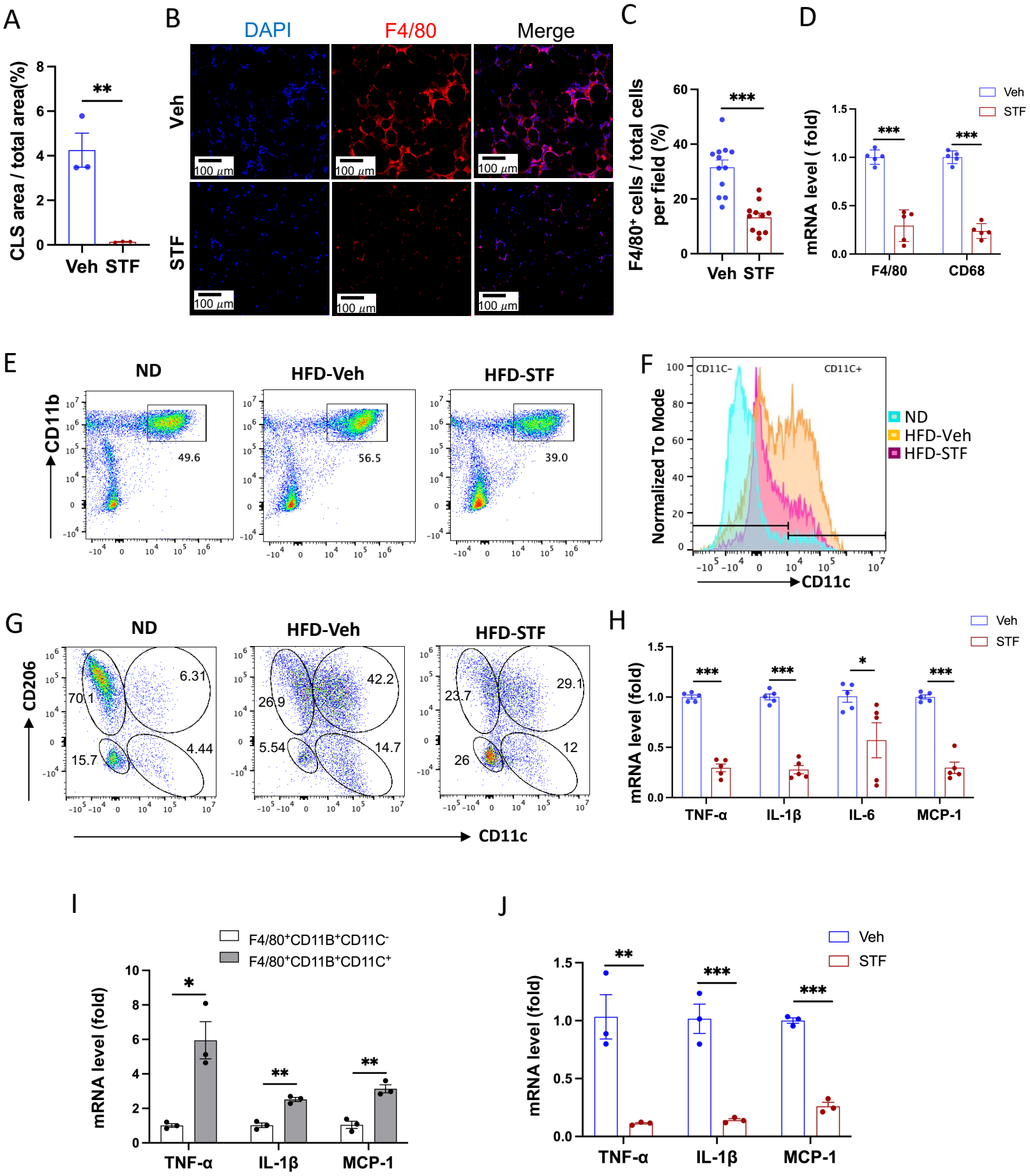
A
CLS area / total area(%)
**
Veh STF
B
DAPI
F4/80
Merge
Veh
STF
100 μm
C
F4/80⁺ cells / total cells per field (%)
***
Veh STF
D
mRNA level (fold)
Veh
STF
***
F4/80
CD68
E
ND
HFD-Veh
HFD-STF
CD11b
49.6
56.5
39.0
F
CD11C-
CD11C+
Normalized To Mode
ND
HFD-Veh
HFD-STF
CD11c
G
ND
HFD-Veh
HFD-STF
CD206
70.1
6.31
15.7
4.44
26.9
42.2
5.54
14.7
23.7
29.1
26
12
CD11c
H
mRNA level (fold)
Veh
STF
TNF-α
IL-1β
IL-6
MCP-1
I
F4/80⁺CD11B⁺CD11C⁻
F4/80⁺CD11B⁺CD11C⁺
mRNA level (fold)
TNF-α
IL-1β
MCP-1
J
Veh
STF
mRNA level (fold)
TNF-α
IL-1β
MCP-1

Fig. 5

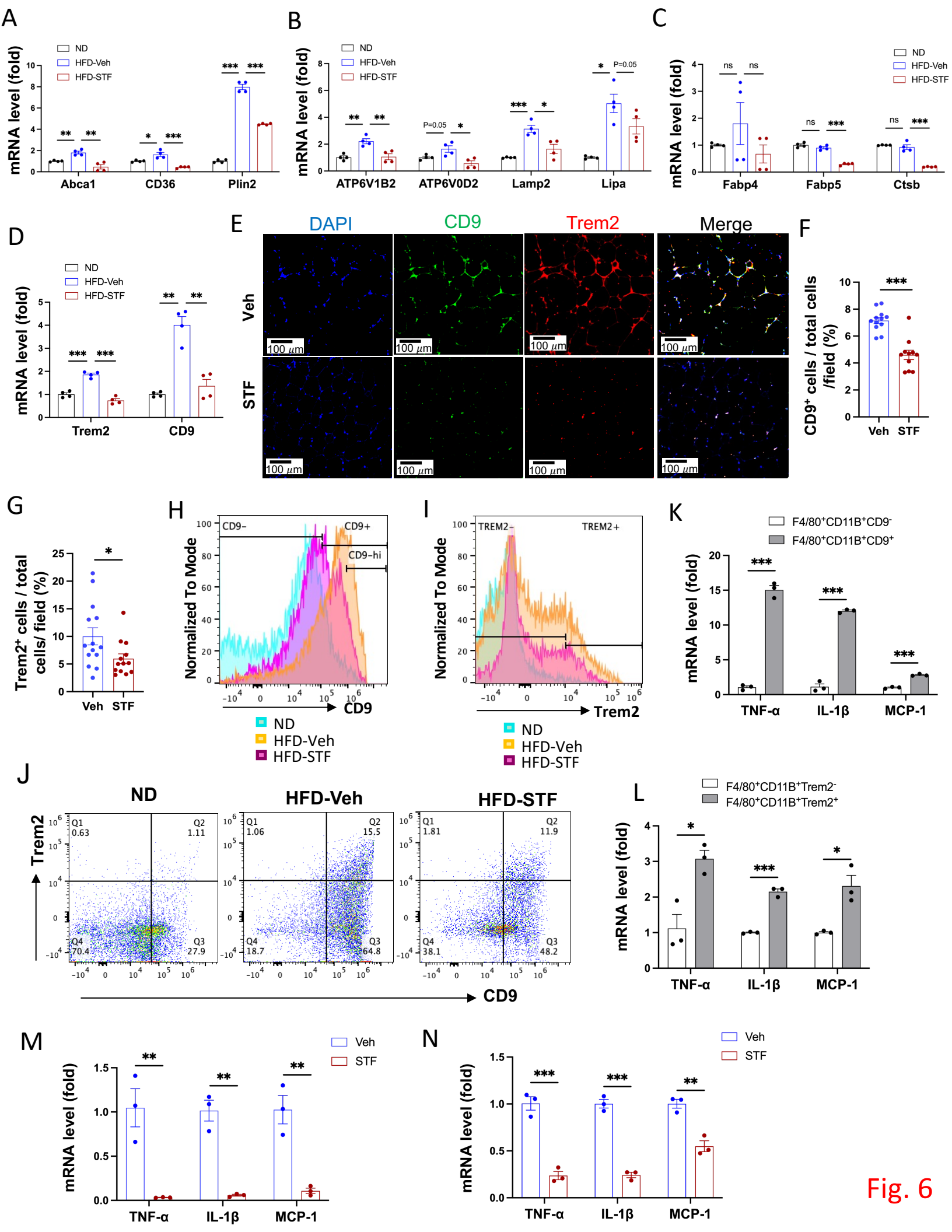
A
ND
HFD-Veh
HFD-STF
mRNA level (fold)
Abca1
CD36
Plin2
B
ATP6V1B2
ATP6V0D2
Lamp2
Lipa
P=0.05
C
Fabp4
Fabp5
Ctsb
ns
D
Trem2
CD9
E
DAPI
CD9
Trem2
Merge
Veh
STF
100 μm
F
CD9⁺ cells / total cells /field (%)
Veh
STF
G
Trem2⁺ cells / total cells/ field (%)
H
CD9−
CD9+
CD9−hi
Normalized To Mode
CD9
I
TREM2−
TREM2+
Trem2
J
ND
HFD-Veh
HFD-STF
Trem2
CD9
Q1 0.63
Q2 1.11
Q4 70.4
Q3 27.9
Q1 1.06
Q2 15.5
Q4 18.7
Q3 64.8
Q1 1.81
Q2 11.9
Q4 38.1
Q3 48.2
K
F4/80⁺CD11B⁺CD9⁻
F4/80⁺CD11B⁺CD9⁺
TNF-α
IL-1β
MCP-1
L
F4/80⁺CD11B⁺Trem2⁻
F4/80⁺CD11B⁺Trem2⁺
M
N
Veh
STF

Fig. 6

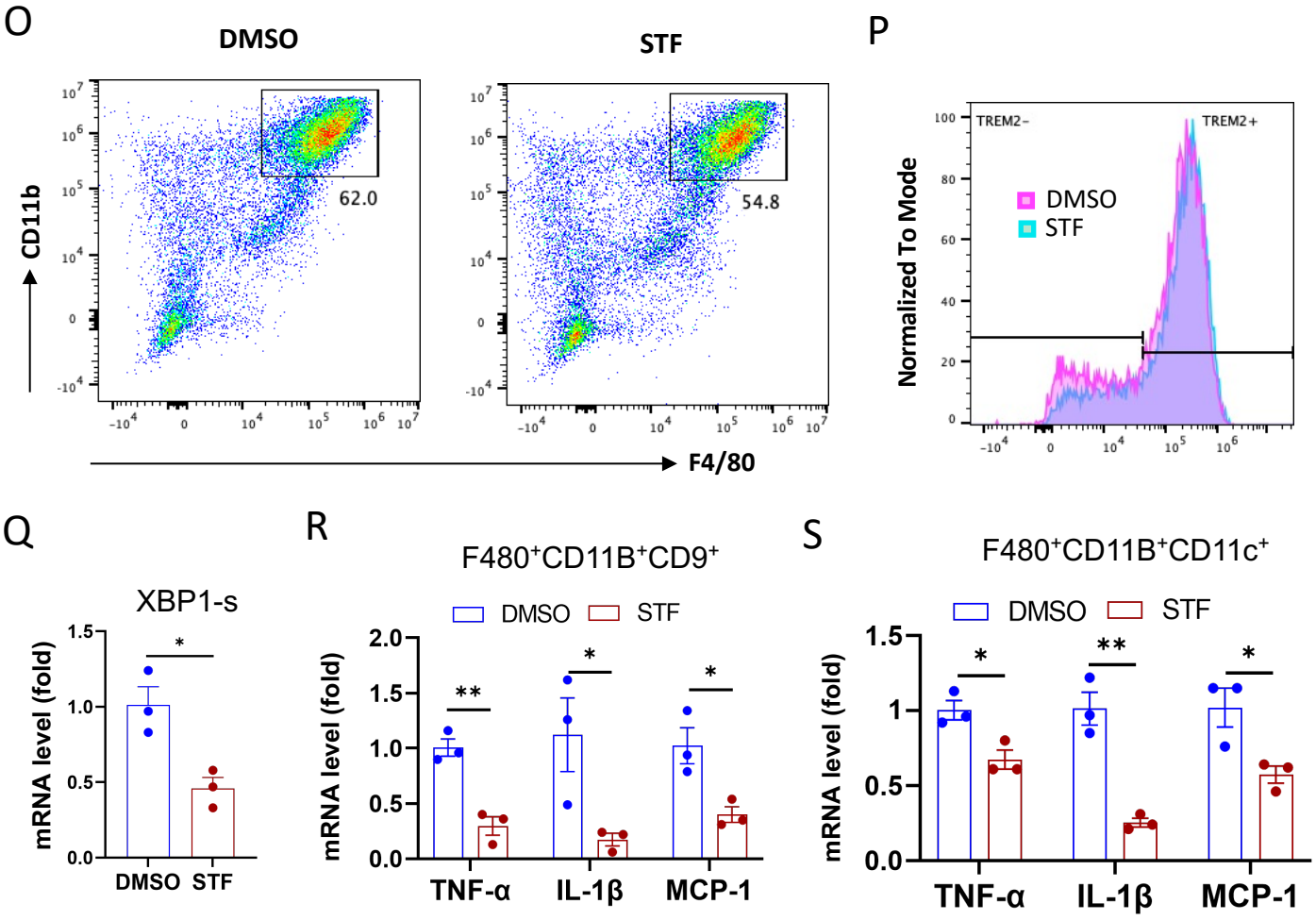
O
DMSO
STF
CD11b
F4/80
62.0
54.8
P
TREM2−
TREM2+
DMSO
STF
Normalized To Mode
Q
XBP1-s
mRNA level (fold)
DMSO
STF
R
F480⁺CD11B⁺CD9⁺
DMSO
STF
mRNA level (fold)
TNF-α
IL-1β
MCP-1
S
F480⁺CD11B⁺CD11c⁺
DMSO
STF
mRNA level (fold)
TNF-α
IL-1β
MCP-1

Fig. 6 cont.

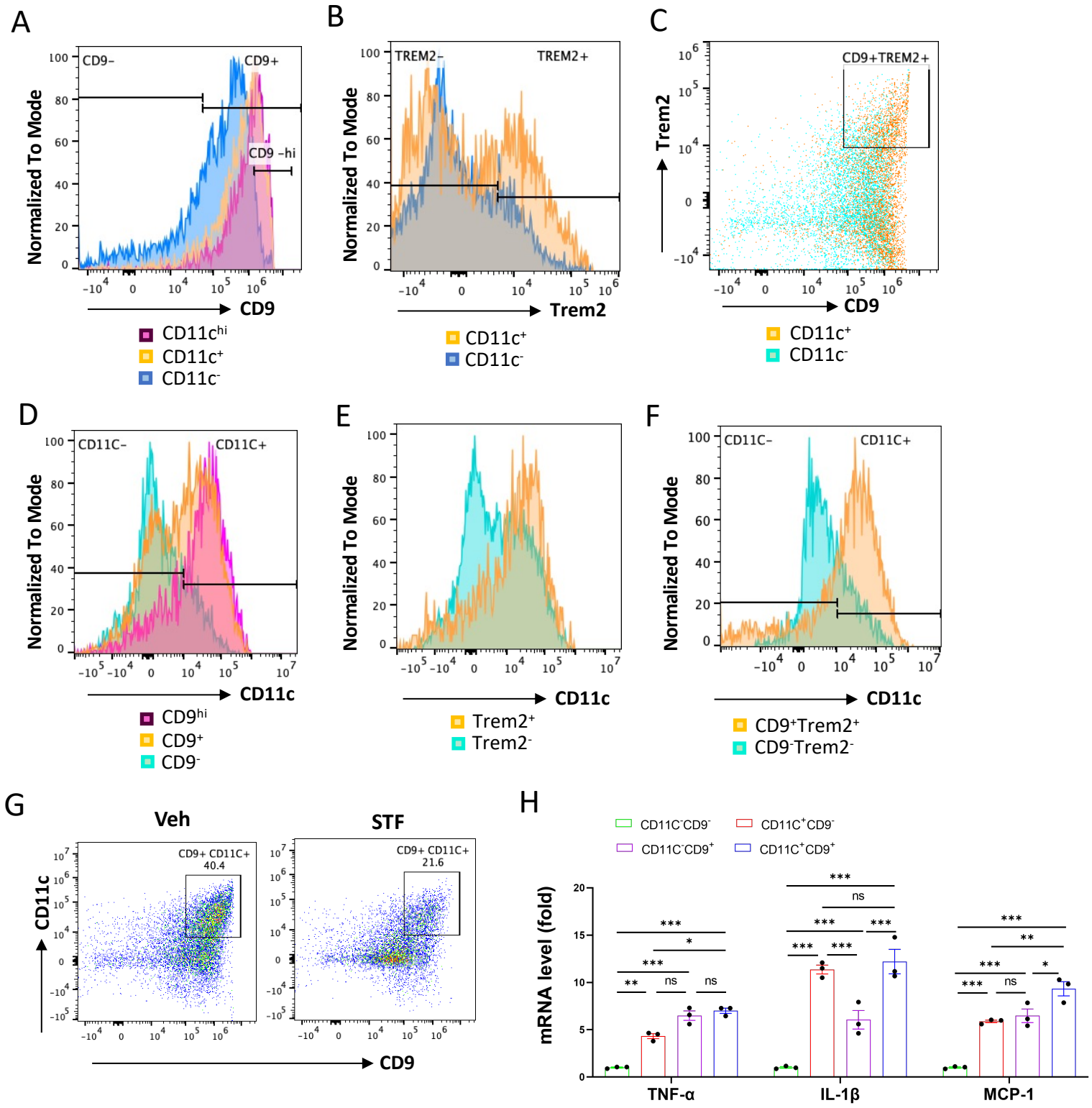
A
CD9−
CD9+
CD9 −hi
Normalized To Mode
CD9
CD11c^hi
CD11c^+
CD11c^-
B
TREM2−
TREM2+
Normalized To Mode
Trem2
CD11c^+
CD11c^-
C
CD9+TREM2+
Trem2
CD9
CD11c^+
CD11c^-
D
CD11C−
CD11C+
Normalized To Mode
CD11c
CD9^hi
CD9^+
CD9^-
E
Normalized To Mode
CD11c
Trem2^+
Trem2^-
F
CD11C−
CD11C+
Normalized To Mode
CD11c
CD9^+Trem2^+
CD9^-Trem2^-
G
Veh
STF
CD9+ CD11C+
40.4
CD9+ CD11C+
21.6
CD11c
CD9
H
CD11C^-CD9^-
CD11C^+CD9^-
CD11C^-CD9^+
CD11C^+CD9^+
mRNA level (fold)
TNF-α
IL-1β
MCP-1

Fig. 7

Table 1

Table 1a

F4/80$^+$CD11B$^+$		
	Total cell#/eWAT/mouse	Cell#/g of eWAT/mouse
ND	0.29 ± 0.25 x 10^5	0.62 ± 0.45 x 10^5
HFD-Veh	1.43 ± 0.086 x 10^6	0.77 ± 0.015 x 10^6
HFD-STF	0.76 ± 0.13 x 10^6	0.36 ± 0.018 x 10^6
HFD-Veh/ND: Fold (P value)	49.63 (0.0041)	12.54 (0.0045)
HFD-STF/HFD-Veh: Fold (P value)	0.54 (0.053)	0.46 (0.0033)

Table 1b

F4/80$^+$CD11B$^+$CD11C$^+$			
	Percentage	Total cell#/eWAT/mouse	Cell#/g of eWAT/mouse
ND	14.59 ± 6.92	0.25 ± 0.16 x10^4	0.59 ± 0.23 x10^4
HFD-Veh	52.95 ± 11.25	0.75 ± 0.11 x10^6	4.11 ± 0.96 x10^5
HFD-STF	37.65 ± 12.65	0.27 ± 0.05 x10^6	1.32 ± 0.38 x10^5
HFD-Veh/ND: Fold (P value)	3.63 (0.007)	299.58 (0.00036)	70.06 (0.0018)
HFD-STF/HFD-Veh: Fold (P value)	0.71 (0.19)	0.36 (0.0027)	0.32 (0.009)

Table 1c

F4/80$^+$CD11B$^+$CD11C$^+$CD206$^+$			
	Percentage	Total cell#/eWAT/mouse	Cell#/g of eWAT/mouse
ND	13.46 ± 7.15	0.21 ± 0.13 x10^4	0.63 ± 0.27 x10^4
HFD-Veh	50.45 ± 8.25	7.13 ± 0.74 x10^5	4.19 ± 0.05 x10^5
HFD-STF	38.25 ± 9.15	2.80 ± 0.19 x10^5	1.35 ± 0.07 x10^5
HFD-Veh/ND: Fold (P value)	3.75 (0.0042)	337.56 (7.79E-05)	75.0 (0.0008)
HFD-STF/HFD-Veh: Fold (P value)	0.76 (0.16)	0.39 (0.00062)	0.35 (0.0049)

Table 1d

F4/80$^+$CD11B$^+$CD206$^+$CD11C$^-$			
	Percentage	Total cell#/eWAT/mouse	Cell#/g of eWAT/mouse
ND	72.35 ± 2.25	2.03 ± 1.72 x10^4	4.36 ± 3.13 x10^4
HFD-Veh	23.35 ± 3.55	3.37 ± 0.71 x10^5	1.80 ± 0.24 x10^5
HFD-STF	28.95 ± 5.25	2.14 ± 0.017 x10^5	1.02 ± 0.13 x10^5
HFD-Veh/ND: Fold (P value)	0.32 (3.55E-05)	16.61 (0.0017)	4.13 (0.0038)
HFD-STF/HFD-Veh: Fold (P value)	1.24 (0.20)	0.64 (0.40)	0.57 (0.0076)

Table 2

Table 2a

F4-80$^+$CD11B$^+$CD9$^+$			
	Percentage	Total cell#/eWAT/mouse	Cell#/g of eWAT/mouse
ND	23.25 ± 8.75	0.45 ± 0.32 x10^4	1.04 ± 0.51 x10^4
HFD-Veh	72.70 ± 2.60	1.04 ± 0.026 x10^6	0.56 ± 0.032 x10^6
HFD-STF	55.50 ± 13.20	0.41 ± 0.027 x10^6	0.20 ± 0.037 x10^6
HFD-Veh/ND: Fold (P value)	3.13 (0.032)	228.14 (0.00062)	54.08 (0.0034)
HFD-STF/HFD-Veh: Fold (P value)	0.77 (0.16)	0.39 (0.0035)	0.35 (0.017)

Table 2b

F4-80$^+$CD11B$^+$Trem2$^+$			
	Percentage	Total cell#/eWAT/mouse	Cell#/g of eWAT/mouse
ND	13.33 ± 11.58	0.98 ± 0.046 x10^3	2.99 ± 1.12 x10^3
HFD-Veh	21.60 ± 5.00	3.04 ± 0.52 x10^5	1.68 ± 0.42 x10^5
HFD-STF	16.70 ± 2.80	1.24 ± 0.06 x10^5	0.59 ± 0.07 x10^5
HFD-Veh/ND: Fold (P value)	1.62 (0.32)	309.97 (0.00056)	56.13 (0.0024)
HFD-STF/HFD-Veh: Fold (P value)	0.77 (0.21)	0.41 (0.0040)	0.35 (0.011)

Table 2c

F4-80$^+$CD11B$^+$CD9$^+$Trem2$^+$			
	Percentage	Total cell#/eWAT/mouse	Cell#/g of eWAT/mouse
ND	7.56 ± 6.45	0.59 ± 0.0090 x10^3	1.75 ± 0.56 x10^3
HFD-Veh	19.95 ± 4.45	2.81 ± 0.46 x10^5	1.55 ± 0.37 x10^5
HFD-STF	14.45 ± 2.55	1.07 ± 0.0041 x10^5	0.51 ± 0.065 x10^5
HFD-Veh/ND: Fold (P value)	2.64 (0.052)	479.54 (0.00047)	88.59 (0.0021)
HFD-STF/HFD-Veh: Fold (P value)	0.72 (0.14)	0.38 (0.0029)	0.33 (0.0092)

Table 3

Table 3a

Percentage of cells expressing	CD9	Trem2	CD9, Trem2
F4/80^{+}CD11b^{+}CD11c^{+}	91.30 ± 0.40	43.55 ± 8.65	30.05 ± 5.55
F4/80^{+}CD11b^{+}CD11c^{-}	70.40 ± 1.0	24.35 ± 4.05	8.35 ± 1.86
P value	0.0027	0.074	0.066

Table 3b

	CD9+	CD9-	Trem2+	Trem2-	CD9+Trem2+	CD9-Trem2-
Percentage of CD11c+	63.25 ± 10.85	29.90 ± 9.1	78.25 ± 12.35	49.55 ± 9.85	78.65 ± 13.05	24.60 ± 5.90
P value	0.14		0.21		0.063	

Table 3c

F4-80^{+}CD11B^{+}CD9^{+}CD11c^{+}			
	Percentage	Total cell #/mouse	Cell #/fat weight (g)
ND	8.16 ± 3.24	0.16 ± 0.11 x10^{4}	0.36 ± 0.17 x10^{4}
HFD-Veh	45.45 ± 5.05	6.45 ± 0.33 x10^{5}	3.52 ± 0.46 x10^{5}
HFD-STF	29.40 ± 7.80	2.14 ± 0.21 x10^{5}	1.03 ± 0.23 x10^{5}
HFD-Veh/ND: Fold (P value)	5.57 (0.025)	416.29 (0.0026)	98.75 (0.017)
HFD-STF/HFD-Veh: Fold (P value)	0.65 (0.23)	0.33 (0.008)	0.29 (0.040)

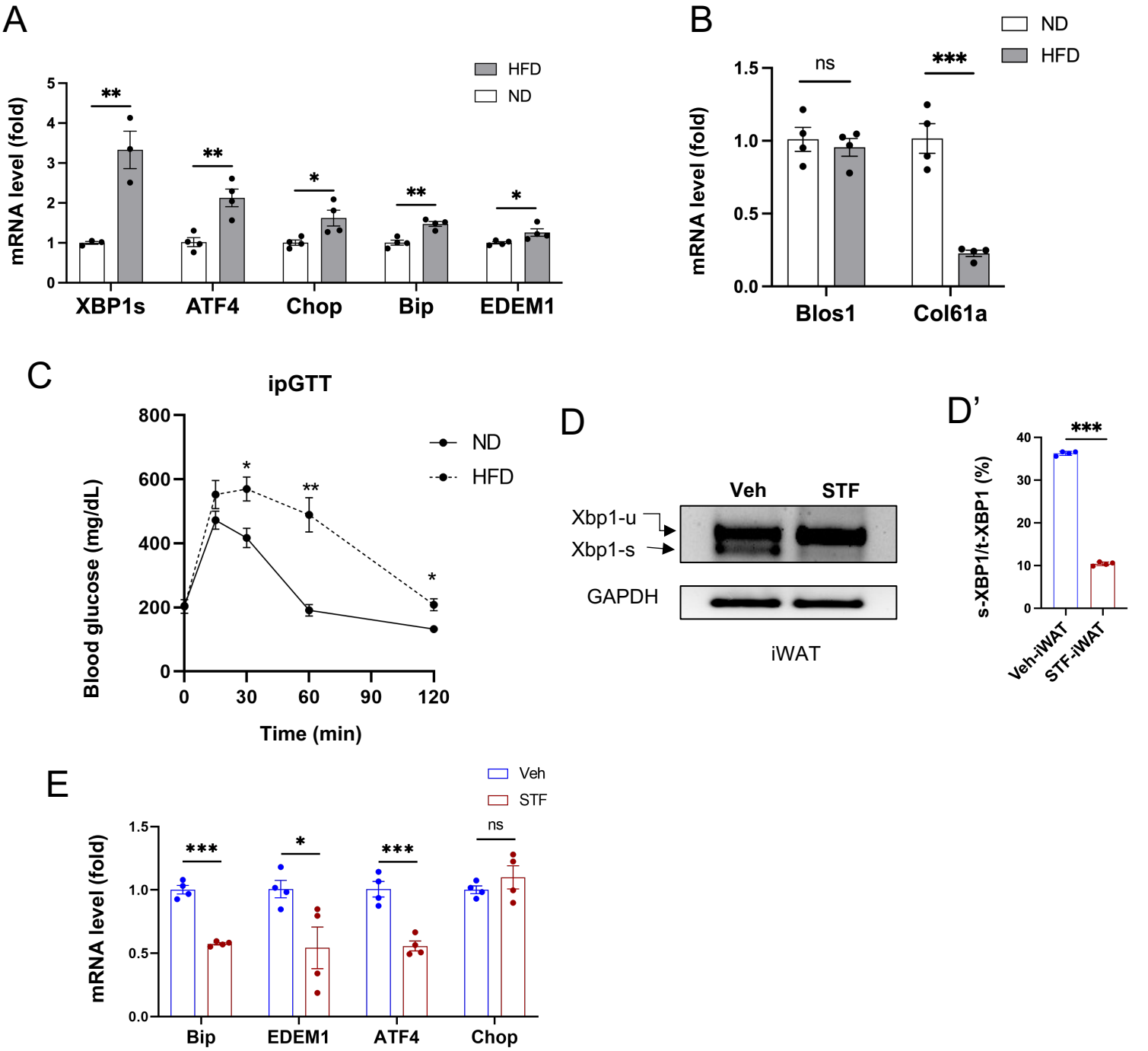

S Figure 1. ER stress and IRE1α activation in adipose tissues in DIO mice. A-B. mRNA levels of ER stress genes (A) and of IRE1α RIDD target genes (B) in the eWAT from mice fed ND (normal diet) and HFD for 14 weeks, assessed by qRT-PCR. The results are expressed as fold change and are representative of 3 independent experiments. C. Glucose tolerance test performed on mice on ND and HFD for 8 weeks. Blood glucose levels measured at indicated time points after intraperitoneal injection of glucose (1.5 g/kg body weight) following 6-h fasting. D-D'. XBP1 mRNA levels were analyzed from eWAT of DIO mice treated with vehicle or STF by RT-PCR and resolved by agarose gel electrophoresis. The full length (unspliced, XBP1-u) and spliced (XBP1-s) forms of XBP1 mRNA were indicated (D) and quantified (D'). GAPDH mRNA was used as an internal control. The data shown are representative of 3 independent experiments. E. mRNA levels for indicated genes were analyzed in eWAT of DIO mice treated with vehicle or STF by qRT-PCR. The results are expressed as fold change and are representative of 3 independent experiments. Data are expressed as mean ± SEM. $*P < 0.05$, $**P < 0.01$, and $***P < 0.001$.

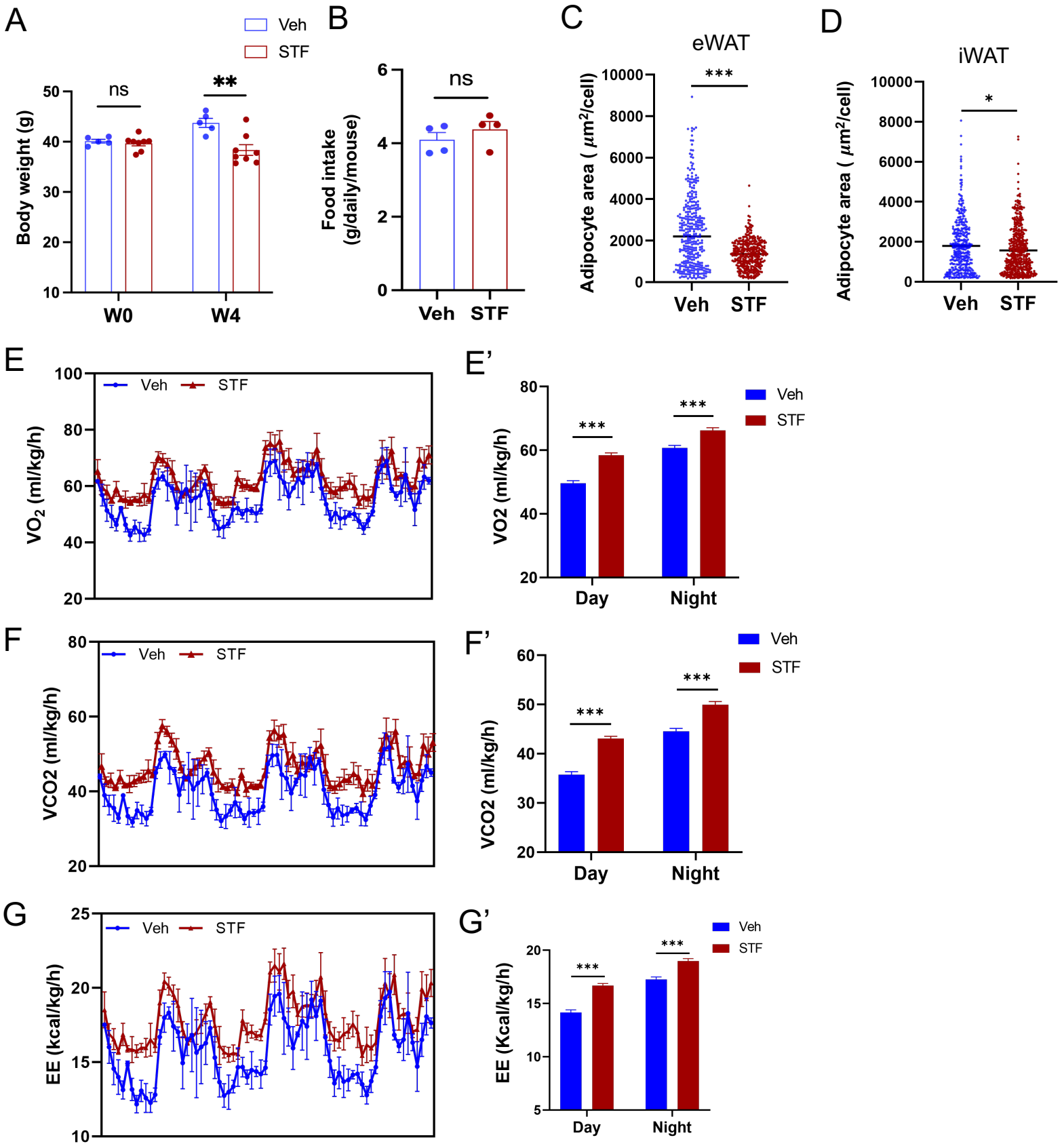

S Figure 2. STF protects against diet-induced obesity and promotes energy expenditure. A. Body weight of DIO mice treated with vehicle (n=5) or STF (n=8) before and after treatment for 4 weeks. B. Daily food intake from DIO mice treated with vehicle or STF, measured for three consecutive days. C-D. Adipocyte area per cell in the sections of eWAT (C) and iWAT (D). E-E'. Curves (E) and quantification (E') of oxygen consumption levels. F-F'. Curves (F) and quantification (F') of CO2 production levels. G-G'. Curves (G) and quantification (G') of energy expenditure levels calculated. For E-G', the data was normalized by body weight for analysis for group effect. Data were represented as mean ± SEM and analyzed using the unpaired two-tailed Student's t-test between two samples or ANOVA with multiple comparisons . $*P < 0.05$, $**P < 0.01$, and $***P < 0.001$.

Suppl. Fig. 2

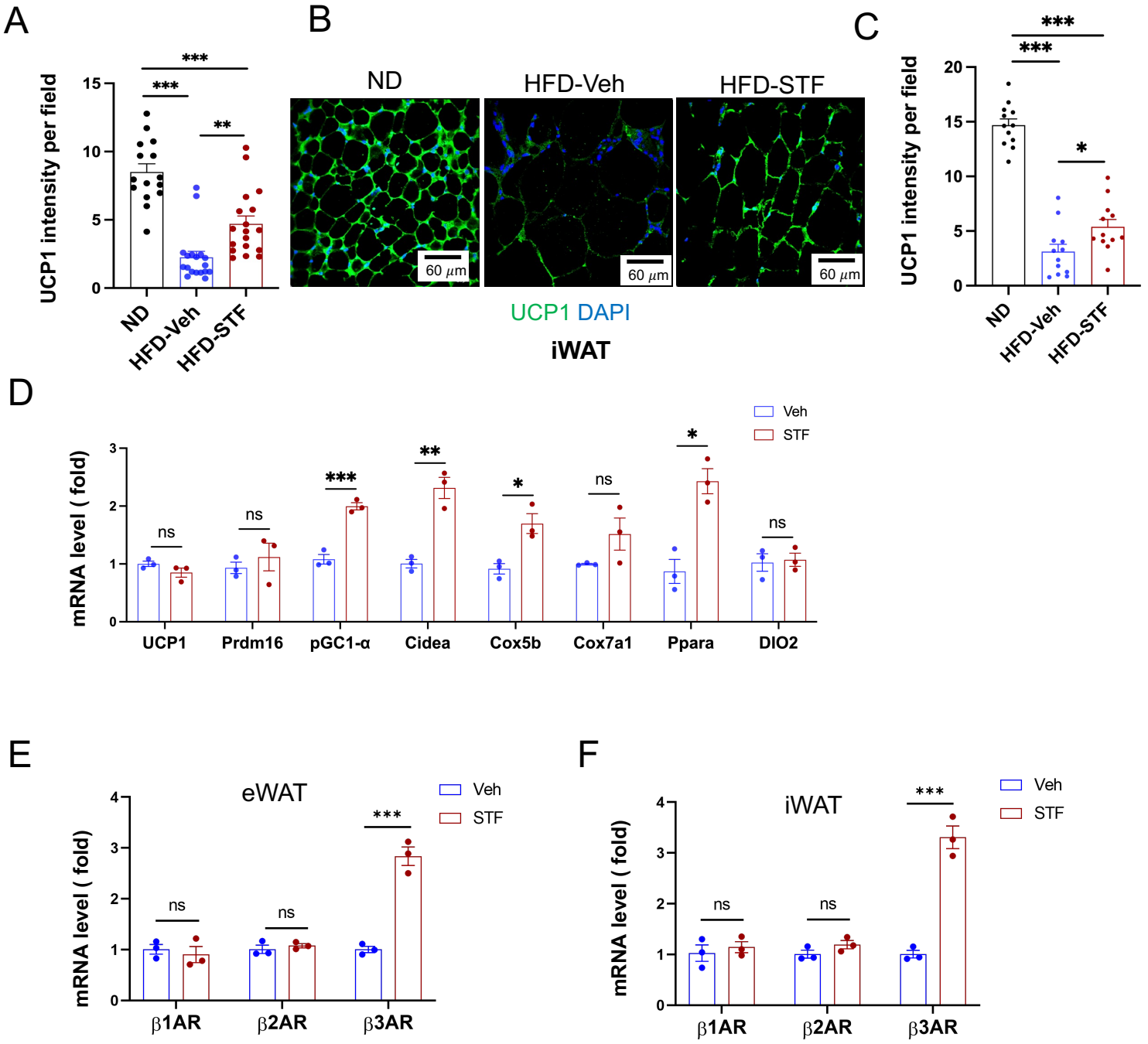

S Figure 3. STF promotes thermogenesis in WAT of DIO mice. A. Quantification of immune-signal intensity of UCP1 in eWAT sections from ND mice and DIO mice treated with vehicle or STF. B-C. UCP1 immunofluorescence staining of iWAT sections from ND-fed mice and DIO mice treated with vehicle or STF. Representative images of UCP1 immunofluorescence staining of iWAT (B) and quantification of immune-signal intensity of UCP1 (C). D. mRNA levels of thermogenic genes in iWAT from DIO mice treated with vehicle or STF, assessed by qRT-PCR. The results are expressed as fold change and are representative of 3 independent experiments. E-F. mRNA levels of β-adrenoceptor genes in eWAT (E) and iWAT (F) from DIO mice treated with vehicle or STF, assessed by qRT-PCR. The results are expressed as fold change and are representative of 3 independent experiments. Data are the mean ± SEM. $*P < 0.05$, $**P < 0.01$, and $***P < 0.001$.

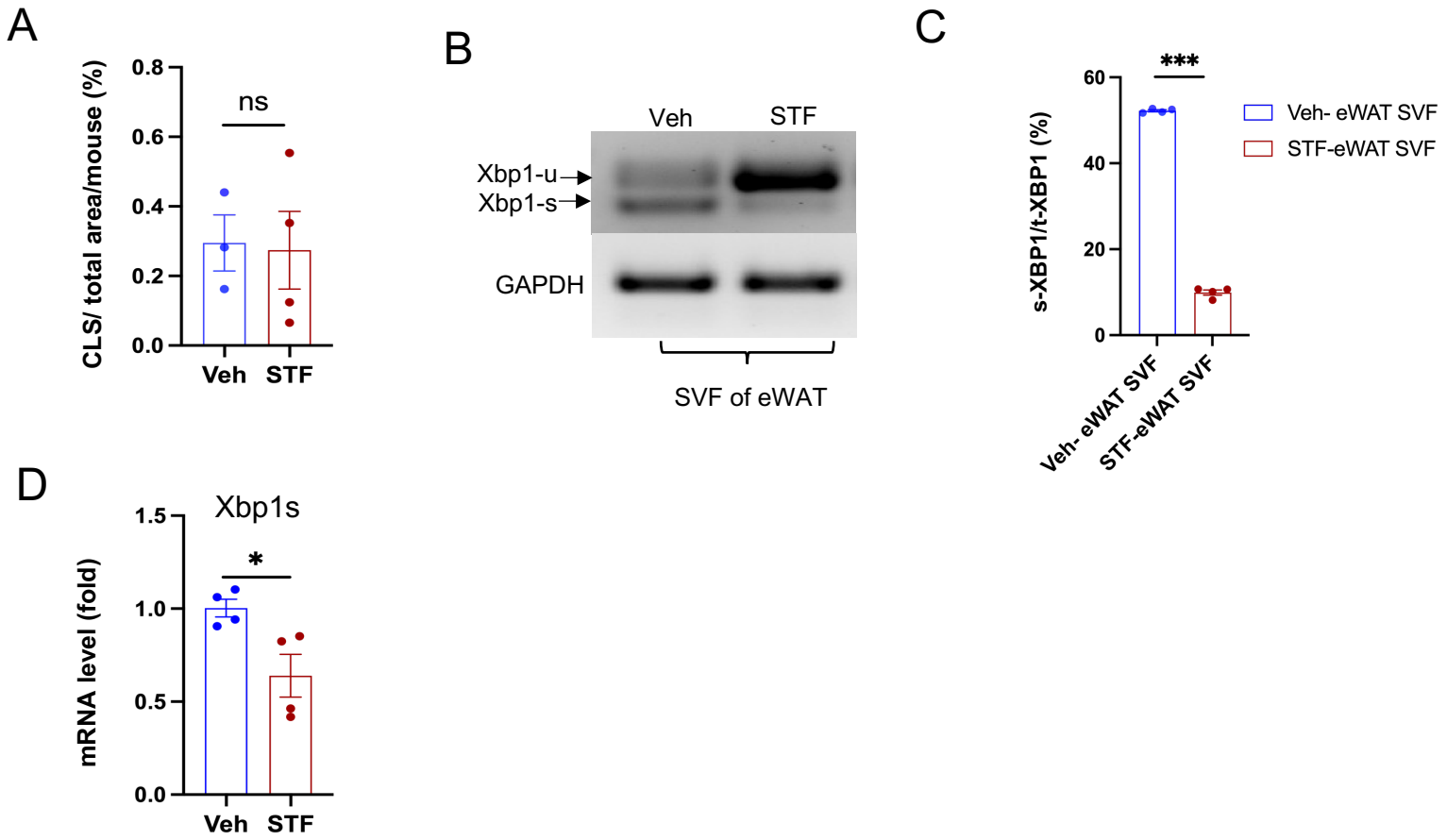

S Figure 4. STF inhibits IRE1α activity in the SVF of obese eWAT. A. Percentage of CLS area in iWAT sections from DIO mice treated with vehicle or STF. B-C. Splicing of XBP1 mRNA was analyzed from the SVFs of eWAT of DIO mice treated with vehicle or STF by RT-PCR and resolved by agarose gel electrophoresis. The full length (unspliced, XBP1-u) and spliced (XBP1-s) forms of XBP1 mRNA were indicated (B) and quantified with t-XBP1 as the sum of XBP1-u and XBP1-s (C). GAPDH mRNA was used as an internal control. The data shown are representative of 3 independent experiments. D. mRNA levels for indicated genes were analyzed in the SVFs of eWAT of DIO mice treated with vehicle or STF by qRT-PCR. The results are expressed as fold change and are representative of 3 independent experiments. Data are the mean ± SEM. $*P < 0.05$, $**P < 0.01$, and $***P < 0.001$.

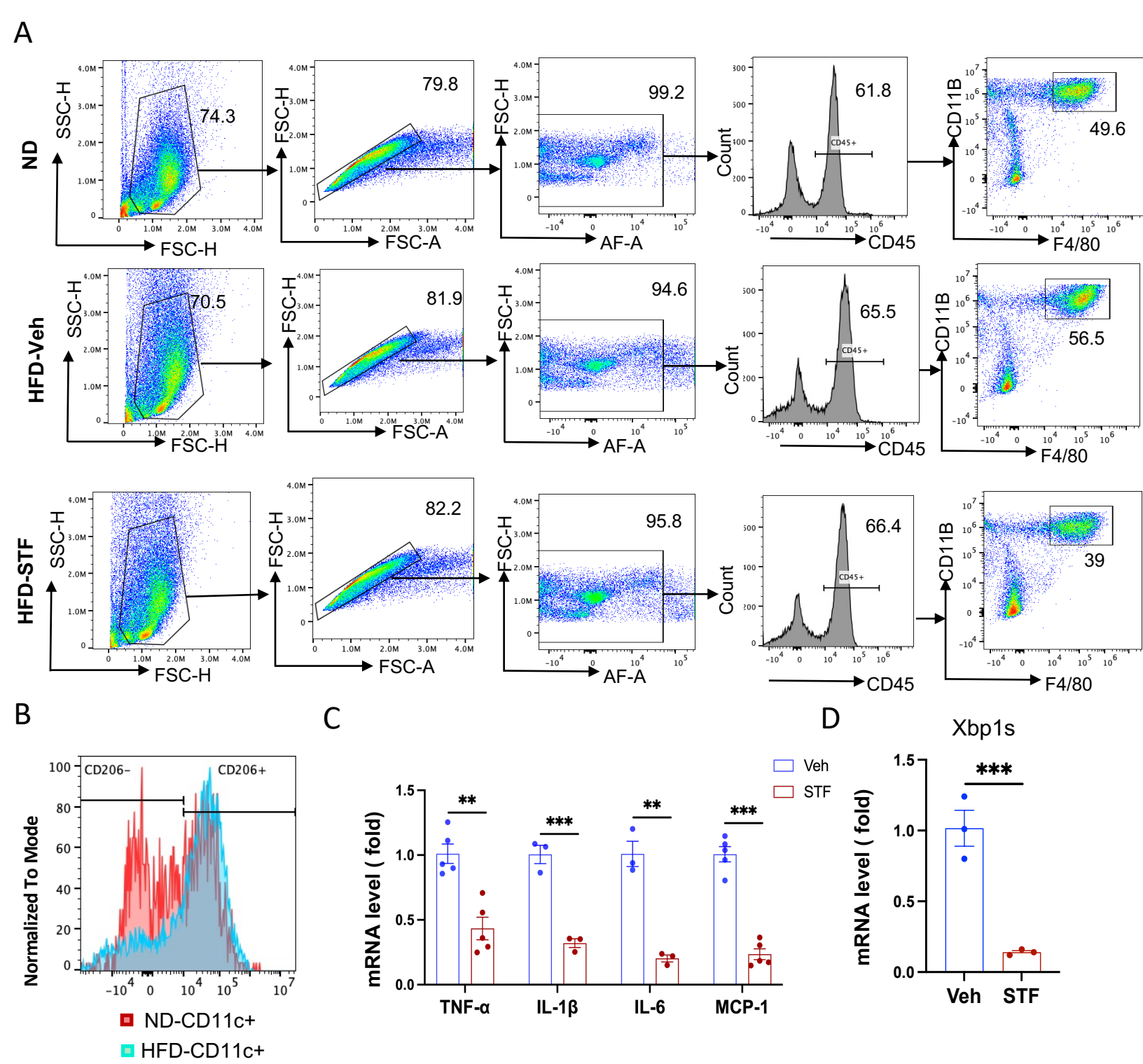
A
ND
HFD-Veh
HFD-STF
SSC-H
FSC-H
FSC-A
AF-A
Count
CD45
CD45+
CD11B
F4/80
74.3
79.8
99.2
61.8
49.6
70.5
81.9
94.6
65.5
56.5
82.2
95.8
66.4
39
B
Normalized To Mode
CD206−
CD206+
ND-CD11c+
HFD-CD11c+
C
mRNA level (fold)
Veh
STF
TNF-α
IL-1β
IL-6
MCP-1
D
Xbp1s
mRNA level (fold)
Veh
STF

Suppl. Fig. 5

S Figure 5. STF suppresses obesity-driven ATM accumulation and adipose inflammation. A. Representative pseudocolor cell density flow cytometry plots showing the gating strategy used for analysis of macrophage subsets ($F4/80^+$ $CD11b^+$) of SVFs of eWAT from ND-fed mice and DIO mice treated vehicle or STF, for figures shown in Fig. 5E. For Fig. 5F, G, I, J, Fig. 6H-N and Fig. 7G, markers were further gated immediately following the steps shown here. Numbers indicate percentage of gated cells. B. Flow cytometry analysis of CD206 signal in $CD11c^+$ ATMs ($F4/80^+CD11b^+CD11C^+$) from eWAT SVFs of mice with an overlay of gated CD206 marker for ND and HFD. Complete gating path follows the strategy shown in A. C. mRNA levels of indicated proinflammatory cytokine/chemokine genes in the SVFs of iWAT of DIO mice treated with vehicle or STF, assessed by qRT-PCR. The results are expressed as fold change and are representative of 3 independent experiments. D. mRNA levels of splice XBP1 in the $CD11C^+$ ATMs ($F4/80^+CD11b^+CD11C^+$) sorted from SVFs of eWAT of DIO mice treated with vehicle or STF, assessed by qRT-PCR. The results are expressed as fold change and are representative of 3 independent experiments. Data are the mean ± SEM. $*P < 0.05$, $**P < 0.01$, and $***P < 0.001$.

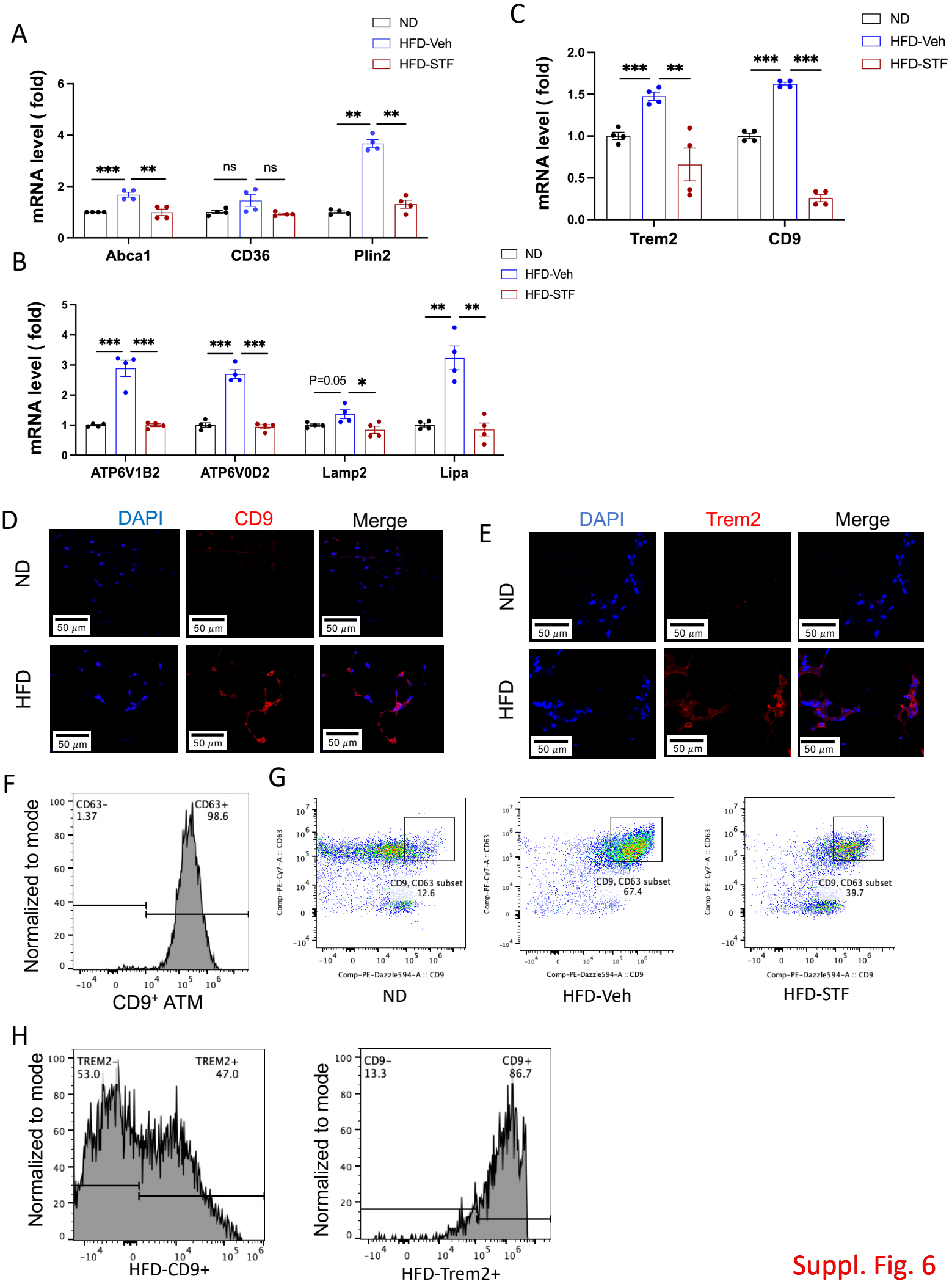
A
ND
HFD-Veh
HFD-STF
mRNA level (fold)
Abca1
CD36
Plin2
***
**
ns
ns
**
**
B
mRNA level (fold)
ATP6V1B2
ATP6V0D2
Lamp2
Lipa
***
***
***
***
P=0.05
*
**
**
C
mRNA level (fold)
Trem2
CD9
***
**
***
***
D
DAPI
CD9
Merge
ND
HFD
50 μm
E
DAPI
Trem2
Merge
ND
HFD
50 μm
F
Normalized to mode
CD63-
1.37
CD63+
98.6
CD9+ ATM
G
CD9, CD63 subset
12.6
CD9, CD63 subset
67.4
CD9, CD63 subset
39.7
Comp-PE-Cy7-A :: CD63
Comp-PE-Dazzle594-A :: CD9
ND
HFD-Veh
HFD-STF
H
Normalized to mode
TREM2-
53.0
TREM2+
47.0
HFD-CD9+
CD9-
13.3
CD9+
86.7
HFD-Trem2+

Suppl. Fig. 6

S Figure 6. STF suppresses metabolically active ATMs in DIO mice. A-C. mRNA levels of indicated genes in the SVFs of iWAT from ND, HFD-veh and HFD-STF mice, assessed by qRT-PCR. The results are expressed as fold change and are representative of 3 independent experiments. D. Representative images of immunofluorescent staining of CD9 (red) in the eWAT sections of ND- and HFD-fed mice. DAPI (blue) for nuclear staining. E. Representative images of immunofluorescent staining of Trem2 (red) in the eWAT sections of ND- and HFD-fed mice. DAPI (blue) for nuclear staining. F. Flow cytometry analysis of CD63 signal in $CD9^+$ ATMs from eWAT SVFs of DIO mice, gated against CD9 and CD63 antibodies sequentially following the gating strategy shown in Supplemental Figure 5A. G. Flow cytometry analysis of $CD9^+$ and $CD63^+$ ATMs from eWAT SVFs of ND, HFD-Veh and HFD-STF mice, gated against CD9 and Trem2 antibodies simultaneously following the gating strategy shown in Supplemental Figure 5A. H. Flow cytometry analyses of Trem2 signal in $CD9^+$ ATMs (left panel) and of CD9 signal in $Trem2^+$ ATMs (right panel) from eWAT SVFs of DIO mice, gated against CD9 and Trem2 antibodies sequentially (left panel) or against Trem2 and CD9 sequentially (right panel) following the gating strategy shown in Supplemental Figure 5A. Data are the mean ± SEM. $*P < 0.05$, $**P < 0.01$, and $***P < 0.001$.

Suppl. Fig. 6 cont.

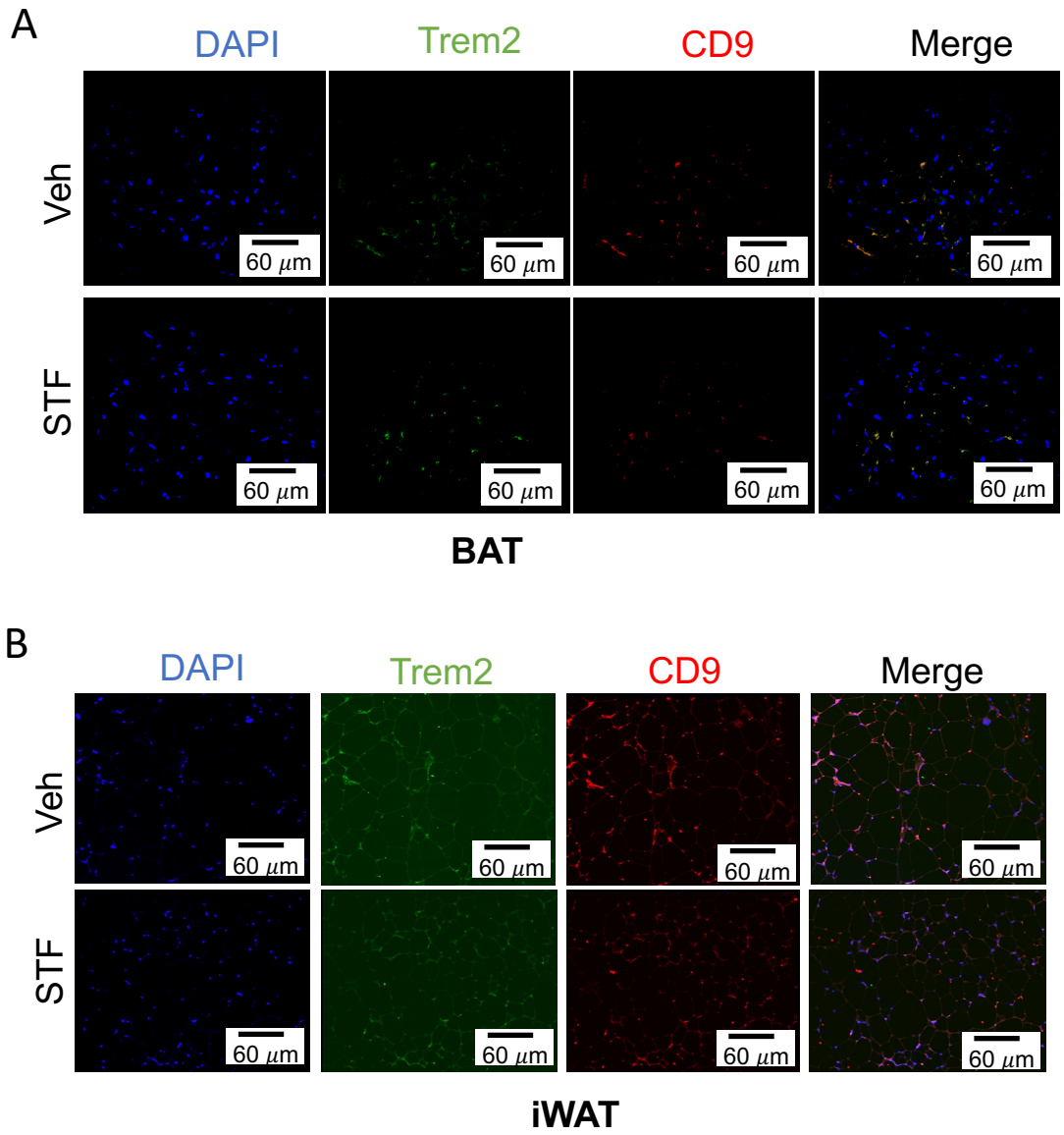

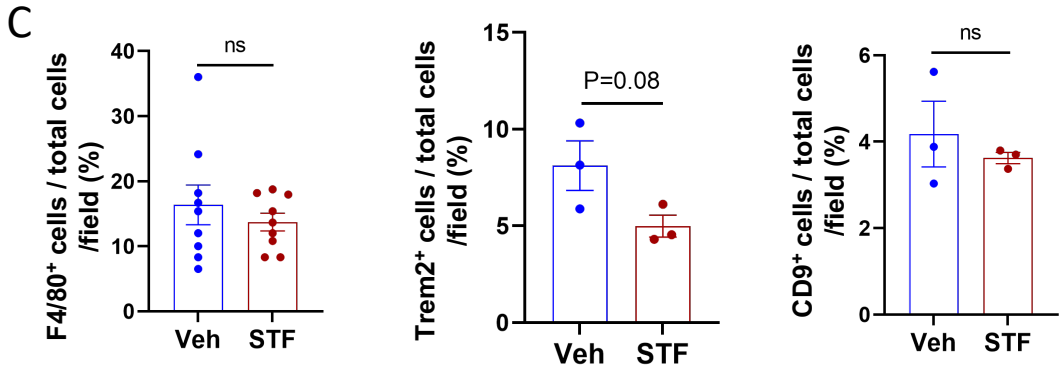

S Figure 7. STF suppresses CD9+ and Trem2+ ATMs in DIO mice. A. Representative images of immunofluorescent staining of CD9 (red) and Trem2 (green) in the BAT sections of HFD-fed mice treated with Veh or STF. DAPI (blue) for nuclear staining. B-C. Representative images of immunofluorescent staining in the iWAT sections of HFD-fed mice treated with Veh or STF (B) and quantification (C). CD9 (red), Trem2 (green), and DAPI for nuclear staining (blue).

Suppl. Fig. 7. New

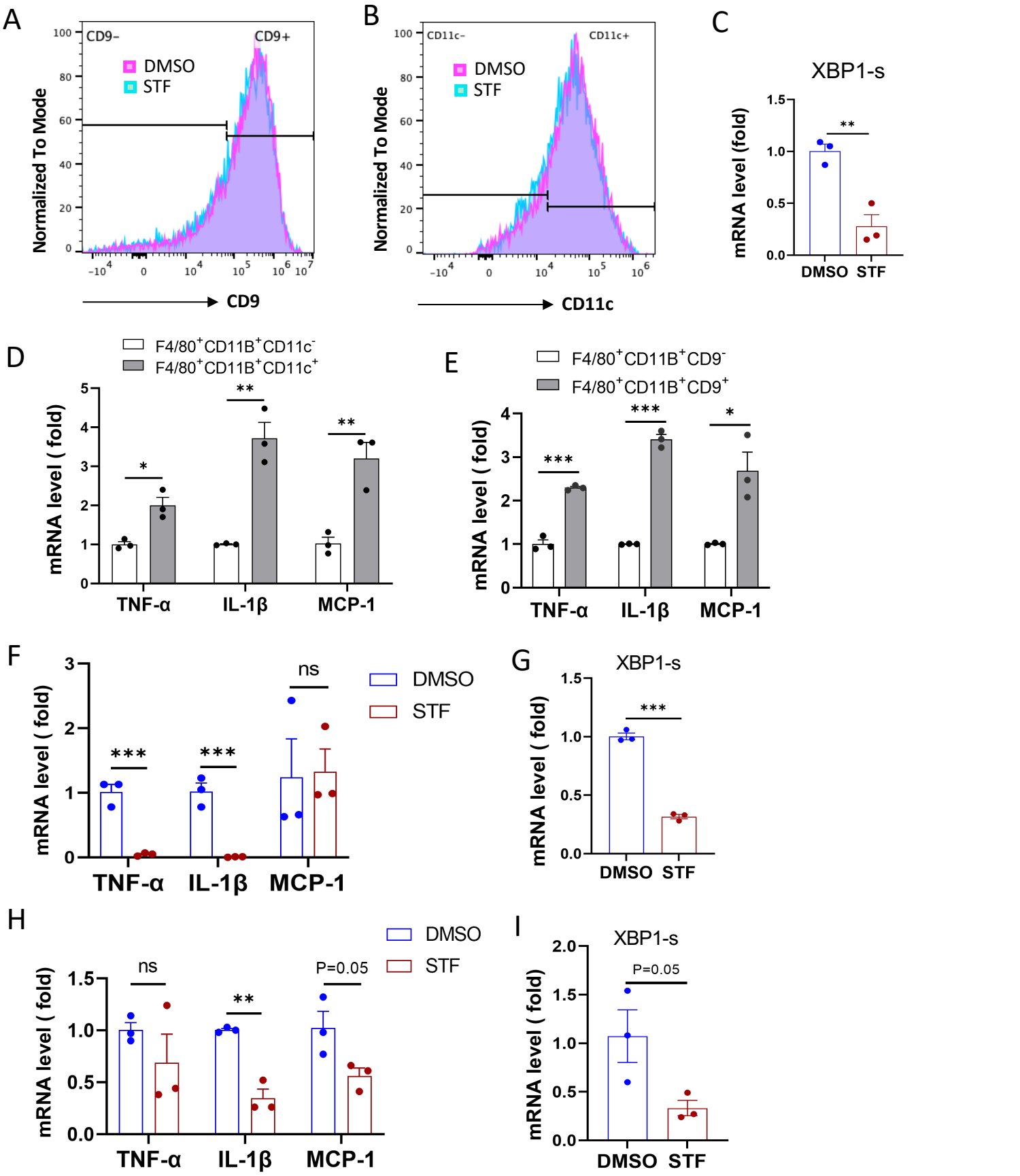

Suppl. Fig. 8. New

S Figure 8. STF suppresses pro-inflammatory cytokines genes expression in ATM in vitro. A-B. Flow cytometry analysis of ATMs from SVFs of the eWAT from 20-week HFD-fed mice. SVFs were cultured and treated with 0.01% DMSO control or STF (30 μM) for 20 h followed by staining and flow analysis, gated against CD9 antibody (A) or CD11C antibody (B). The gating path followed the one as Supplemental Figure 5A. C. mRNA levels of indicated genes in $CD11C^+$ ATMs sorted from SVFs cultured and treated with DMSO or STF, assessed by qRT-PCR. D-E. Comparison of mRNA levels of indicated proinflammatory genes between $CD11C^+$ and $CD11C^-$ ATMs (D) and between $CD9^+$ and $CD9^-$ ATMs (E), sorted from SVFs, assessed by qRT-PCR. F-G. mRNA levels of indicated proinflammatory genes (F) and spliced-XBP1 (G) in $CD9^-$ ATMs sorted from SVFs cultured and treated with DMSO or STF, assessed by qRT-PCR. F-G. mRNA levels of indicated proinflammatory genes (F) and spliced-XBP1 (G) in $CD11C^-$ ATMs sorted from SVFs cultured and treated with DMSO or STF, assessed by qRT-PCR. Data were expressed as mean ± SEM and analyzed using the unpaired two-tailed Student's t-test between two samples or ANOVA with multiple comparisons. $*P < 0.05$, $**P < 0.01$, and $***P < 0.001$..

Suppl. Fig. 8. New. Cont.

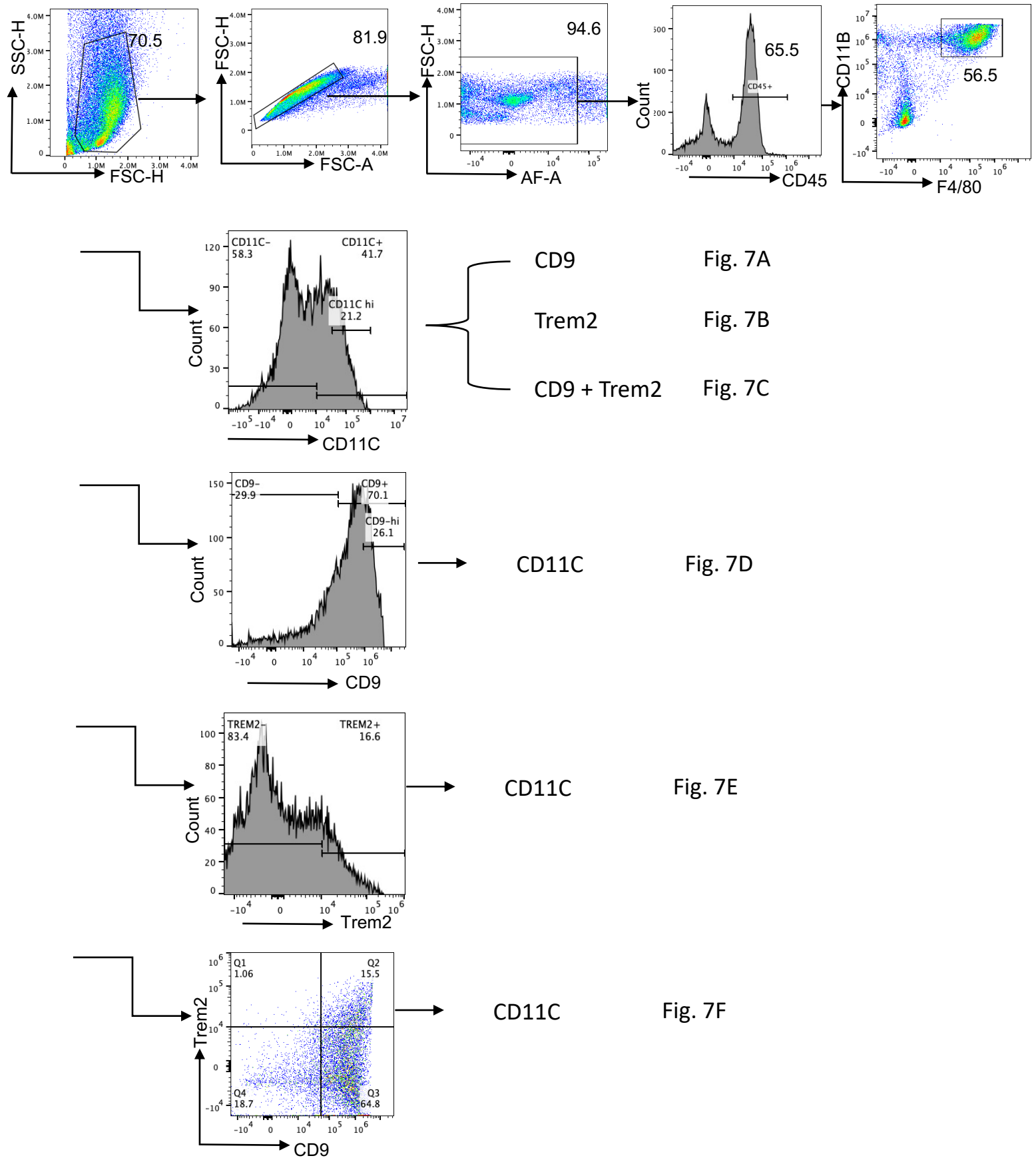

S Figure 9. Flow cytometry analysis strategy related to Figure 7.
Representative pseudocolor cell density flow cytometry plots showing the gating strategy used for analysis of subsets of ATMs in the eWATs from DIO mice with the total F4/80⁺ CD11b⁺ at the top row, followed by the steps specifically for Fig. 7A-F. Numbers indicate percentage of gated cells.

Suppl. Fig. 9

Table S1

Table S1a

F4/80$^+$CD11B$^+$CD11C$^+$CD206$^-$		
	Total cell#/eWAT/mouse	Cell#/g of eWAT/mouse
ND	0.12 ± 0.11 x10^4	0.25 ± 0.23 x10^4
HFD-Veh	1.43 ± 0.79 x10^5	0.74 ± 0.37 x10^5
HFD-STF	0.65 ± 0.43 x10^5	0.28 ± 0.17 x10^5
HFD-Veh/ND: Fold (P value)	118.61 (0.036)	30.27 (0.027)
HFD-STF/HFD-Veh: Fold (P value)	0.45 (0.20)	0.38 (0.12)

Table S1b

F4/80$^+$CD11B$^+$CD206$^-$CD11C$^-$		
	Total cell#/eWAT/mouse	Cell#/g of eWAT/mouse
ND	0.42 ± 0.42 x10^4	0.84 ± 0.83 x10^4
HFD-Veh	0.71 ± 0.13 x10^5	0.38 ± 0.038 x10^5
HFD-STF	1.30 ± 1.03 x10^5	0.56 ± 0.41 x10^5
HFD-Veh/ND: Fold (P value)	16.97 (0.038)	4.54 (0.084)
HFD-STF/HFD-Veh: Fold (P value)	1.83 (0.63)	1.46 (0.71)

Table S1c

F4-80$^-$CD11B$^-$		
	Total cell#/eWAT/mouse	Cell#/g of eWAT/mouse
HFD-Veh	7.04 ± 1.17 x10^5	3.78 ± 0.33 x10^5
HFD-STF	9.28 ± 1.57 x10^5	4.32 ± 0.20 x10^5
HFD-STF/HFD-Veh: Fold (P value)	1.32 (0.37)	1.14 (0.29)

Table S1. Effect of STF treatment on "M1-like" and "M2-like" ATMs in obesity. The total cell number and density of populations from CD11C$^+$CD206$^-$ ATMs in the eWATs of mice with ND, HFD-Veh, or HFD-STF (a), CD11C$^-$CD206$^-$ ATMs in the eWATs of mice with ND, HFD-Veh, or HFD-STF (b), and F4/80$^-$CD11B$^-$ ATMs in the eWATs of DIO mice treated with Veh or STF (c). Data in a-c were obtained from 2 batches of 4-5 mice each and are the mean ± SEM. $*P < 0.05$, $**P < 0.01$, and $***P < 0.001$

Table S2

Table S2

F4-80$^+$CD11B$^+$CD9$^+$CD63$^+$			
	Percentage	Total cell#/eWAT/mouse	Cell#/g of eWAT/mouse
ND	18.00 ± 5.40	0.38 ± 0.29 x10^4	0.87 ± 0.48 x10^4
HFD-Veh	65.90 ± 1.50	9.42 ± 0.78 x10^5	5.09 ± 0.011 x10^5
HFD-STF	49.35 ± 9.65	3.65 ± 0.08 x10^5	1.74 ± 0.25 x10^5
HFD-Veh/ND: Fold (P value)	3.66 (0.013)	245.23 (0.0069)	58.86 (9.59E-05)
HFD-STF/HFD-Veh: Fold (P value)	0.75 (0.23)	0.39 (0.018)	0.34 (0.0057)

Table S2. Characterization of and the effect of STF treatment on CD9$^+$ ATMs in DIO mice. The percentage, total cell number, and density of populations from CD9$^+$CD63$^+$ ATMs in the eWATs of mice with ND, HFD-Veh, or HFD-STF. Data were obtained from 2 batches of 4-5 mice each and are the mean ± SEM. $*P < 0.05$, $**P < 0.01$, and $***P < 0.001$

Supplemental Table 3
Primer sequences used in this work

Gene	Forward Primer	Reverse Primer
GAPDH	AAAGACTGGAGCCCCACACTCTAC	ATCCCGTATTTCACCTCTGCTTC
XBP1s	GAG TCC GCA GCA GGT	GTG TCA GAG TCC ATG
XBP1u	CGCAGACTGCTCGAGATAGA	CCACAAGGCCGTGAGTTTTC
Chop	GCAGCGACAGAGCCAGAATA	CAAGGTGAAAGGCAGGGACT
Bip	GTGTGTGAGACCAGAACCGT	GCAGTCAGGCAGGAGTCTTA
EDEM1	CAAGTGTGGGTACGCCACG	AAAGAAGCTCTCCATCCGGTC
Blos1	CAAGGAGCTGCAGGAGAAGA	CCAGGAGGGTGAAGTAAGAGG
Col61a	TGCTCAACATGAAGCAGACC	TTGAGGGAGAAAGCTCTGGA
ATF4	CCTATAAAGGCTTGCGGCCA	GCTGGATTTCGTGAAGAGCG
UCP1	CACCTTCCCCCTGGACACT	CCCTAGGACACCTTTATACCT
Prdm16	AGGAGGAGGAGAGAGATTCCG	GTCCGGGTCAGGTTCATACAT
pGC1-α	CCCTGCCATTGTTAAGACC	TGCTGCTGTTCCTGTTTTC
Cidea	ATCACAACTGGCCTGGTTACG	TACTACCCGGTGTCCATTTCT
Cox5b	TGCTACCTCCAAAGGCAGCTTC	CATCGCTGACTCTCGCCTTTGT
Cox7a1	CAGCGTCATGGTCAGTCTGT	AGAAAACCGTGTGGCAGAGA
Cox8b	GAACCATGAAGCCAACGACT	GCGAAGTTCACAGTGGTTCC
Ppara	TTCCCTGTGAACTGACGTTT	CCACCATGTTGGATGGATGTG
DIO2	AGAGTGGAGGCGCATGCT	GGCATCTAGGAGGAAGCTGTT
β1AR	CCGAAAGCAGGTGAATGCAA	AGCCAGTAAGCCATACTAAGCCACA
β2AR	CATTGATGTGTTGTGCGTCA	ACTCGGGCCTTATTCTTGGT
β3AR	CCTTCCGTCGTCTTCTGTGT	AGCCATCAAACCTGTTGAGC
TNF-α	CTGAACTTCGGGGTGATCGG	CTACGACGTGGGCTACAGG
IL-1β	TGCCACCTTTTGACAGTGATG	TGATGTGCTGCTGCGAGATT
IL-6	CACTTCACAAGTCGGAGGCT	CTGCAAGTGCATCATCGTTGT
MCP-1	AGGTCCCTGTCATGCTTCTG	TCTCCAGCCTACTCATTGGGA
Mgl1	CAGATCTGGGGCCGTCAAG	GGGAGGAAATGCATCTGGGT
IL-10	AGGCGCTGTCATCGATTTCT	ATGGCCTTGTAGACACCTTGG
F4/80	TCTGCTTCTGTACAGCCACG	CCTCAGAACCCACAGTGTCC
CD68	TGTTCAGCTCCAAGCCCAAA	GTACCGTCACAACCTCCCTG
Abca1	TAGCAGCACCGTGTCTTGTC	GCGTGTCACTTTCATGGTCG